NTNU – Trondheim
Norwegian University of
Science and Technology

Fatigue Analysis of Flexible Risers

A comparative study of different models for
metal fatigue in flexible risers

Daniel Frøland Svoren

Marine Technology
Submission date: June 2013
Supervisor: Svein Sævik, IMT

Norwegian University of Science and Technology
Department of Marine Technology

Scope as given by the Department of Marine Technology

Master Thesis Spring 2013

Stud. tech. Daniel Frøland Svoren

Fatigue Analysis of Flexible Risers

Utmatningsanalyse av fleksible stigerør

The background for this project is related to metal fatigue of flexible risers. The governing load contribution is normally assumed to be 1st and 2nd order wave and current loads in combination with associated floater motions. In addition VIV may also be a concern. However, wave and VIV require different response models. Whereas, the nature of wave responses is characterized with large response amplitudes which requires a non-linear response model, VIV can be handled by a linear frequency domain model due to small response amplitudes. This project focuses on wave induced fatigue.

The wave fatigue calculation is in most cases performed by a two-step procedure: A global analysis in order to obtain the tension, curvatures or hang-off angles followed by a local stress analysis to transform the global quantities into time series of stress used as basis for calculating the final damage as a Miner sum. The global analysis model may be based on elastic beam elements using the slip bending stiffness or elastoplastic beam elements allowing the stick-slip moment curvature behavior. Further in order to handle the wave statistics either regular or on irregular analysis may be performed. Since the stick-slip transition requires small time steps, irregular wave analysis may become time consuming for such models. Alternatively the stick approach can be applied and the full model used only for the cases where the slip curvature is exceeded.

There are different strategies for local stress analysis:

1. To use analytical models allowing direct transformation of the global time series into time series of stress.
2. To use a filter which is based on the outputs from nonlinear FE analysis of the cross-section and then transform the time series into stress.

Scope as given by the Department of Marine Technology

3. By regular wave global analysis calculate harmonic responses in terms of tension and curvature variation and use this as input to non-linear FE stress analysis.
4. By irregular wave global analysis. As the non-linear FE stress model is too time consuming to allow direct transformation of the global time series, the global responses need to be transformed into classes of regular harmonic tension, curvature or hang-off angle variations prior to transforming into stress.

The present project will adopt the ***item 4*** *strategy and focus on the tensile armor fatigue in the bending stiffener area. The work is to be carried out as follows:*

1. Literature study, including flexible pipe technology in general i.e. pipe manufacture, design, pipe-soil interaction, installation methods and associated design criteria. This is also to include the techniques used to perform irregular response analysis including non-linear finite element methods and non-linear time-domain analysis techniques with focus on the methods applied in computer programs such as ORCAFLEX, RIFLEX and BFLEX.
2. Define a relevant flexible riser scenario in terms of water depth, vessel geometry, vessel RAO, pipe and bending stiffener properties, hydrodynamic coefficients and environmental conditions.
3. Establish a global riser model in RIFLEX, apply appropriate blocking of the scatter diagram into fatigue load cases and perform non-linear, irregular wave dynamic analysis to obtain the riser top dynamic response in terms of hang-off angle, curvature and tension variations.
4. Transform the global responses into classes of tension, curvature and hang-off angle variations.
5. Establish three local analysis models for the cross-section in BFLEX, Model 1 based on the “stub” approach and using curvature and tension as input, Model 2 including a full moment based model (ITCODE31) of the BS section and using hang-off angle and tension as input and Model 3 using the sandwich beam approach (ITCODE 0) and same load input as Model 2.
6. Calculate the fatigue damage in the tensile armor and compare the fatigue damage between the three models

Scope as given by the Department of Marine Technology

7. Conclusions and recommendations for further work

The thesis work assumes that all necessary input data are provided by KOGT Subsea. The work scope may prove to be larger than initially anticipated. Subject to approval from the supervisors, topics may be deleted from the list above or reduced in extent. In the thesis the candidate shall present his personal contribution to the resolution of problems within the scope of the thesis work. Theories and conclusions should be based on mathematical derivations and/or logic reasoning identifying the various steps in the deduction. The candidate should utilize the existing possibilities for obtaining relevant literature.

Thesis format. The thesis should be organized in a rational manner to give a clear exposition of results, assessments, and conclusions. The text should be brief and to the point, with a clear language. Telegraphic language should be avoided. The thesis shall contain the following elements: A text defining the scope, preface, list of contents, summary, main body of thesis, conclusions with recommendations for further work, list of symbols and acronyms, references and (optional) appendices. All figures, tables and equations shall be numerated. The supervisors may require that the candidate, in an early stage of the work, presents a written plan for the completion of the work. The original contribution of the candidate and material taken from other sources shall be clearly defined. Work from other sources shall be properly referenced using an acknowledged referencing system. The report shall be submitted in two copies: signed by the candidate, the text defining the scope included, in bound volume(s), drawings and/or computer prints which cannot be bound should be organized in a separate folder.

Ownership. NTNU has according to the present rules the ownership of the thesis. Any use of the thesis has to be approved by NTNU (or external partner when this applies). The department has the right to use the thesis as if the work was carried out by a NTNU employee, if nothing else has been agreed in advance.

Thesis supervisors are Prof. Svein Sævik (NTNU) and Torgrim Andersen (KOGT Subsea).

Preface

This is a thesis for the degree of MSc. in Marine Construction at the *Department of Marine Technology* at NTNU. The work was undertaken the spring of 2013. I wrote the project in cooperation with my employer, the Subsea division of Kongsberg Oil & Gas Technologies (KOGT). The work took primarily place in Trondheim. Two weeks were spent at the offices of KOGT Subsea in Asker and two weeks at their offices in Rio de Janeiro, Brazil.

My motivation for writing about riser fatigue is that this type of analysis utilizes almost every discipline of construction analysis that I have been taught here in Trondheim. The work has been highly educational for me, and I am proud of the outcome. I have gotten a profound knowledge on RIFLEX and BFLEX.

I wish to extend my gratitude towards the thesis advisors Prof. Sævik and MSc. Torgrim Andersen for their guidance throughout this semester. Prof Sævik provided indispensable advice and discussion around the BFLEX models. I am also grateful for the help that Sr. Scientist Naiquen Ye (MarinTek) provided for the cycle-counting procedure. Finally, I want to thank MSc. Ole Frithjof Ravneberg (KOGT Subsea) for valuable input on RIFLEX and wave scatter diagram blocking.

Stud. Tech. Daniel Frøland Svoren
Trondheim, June 2013.

Abstract

This thesis used different methods to model and predict the fatigue from wave loads on the tensile armor layers in a flexible riser in the bending stiffener area. The additional aim of the thesis was to give the reader an understanding of flexible pipes and risers, and present the necessary theory to understand and complete a dynamic analysis of riser with the finite element method, and how to do lifetime predictions from irregular time series.

Different methodologies exist for fatigue calculations for risers. However, the general approach is to use the wave response from a global riser model, and to apply this to a local model which has a more accurate representation of the pipe's cross-section. The actual fatigue calculations are done using a SN-curve and Miner sum. The variations of the different methods lie in how the models are made, what kind of wave loads the global model is subjected to, and what loads are used and how these loads are transformed in to the local model.

The scenario was a new field development close to the Enchova field located in the Campos Basin off the Coast of Rio De Janeiro. This field will be developed with a *turret moored floating unit* with *lazy-wave riser configuration* at a water depth of 125 meters. The system was modeled with simple tubular elements given the pipe's bending stiffness in slip. An irregular wave analysis using the local wave data

was conducted.

The transformation of the global time series was done using the Rainflow method. The range spectra were divided into 40 bins. Three different local models were made in BFLEX. The first model, M1, was a stub, just a representation of the pipe's cross-section. This is a known approach in the industry. The two last models, M2 and M3, were full sized representations of the bending stiffener, which were submitted to axial and lateral loads by decomposing the tension with the riser's *hang-off angle*. This approach is less used. M2 and M3 used different types of elements. Their difference is in the way the tensile armor layer is represented.

M2 and M3 have shown to give a less conservative result than M1. This can be understood from the fact that M2 and M3 give a more realistic representation of the load history. They capture other effects as well, like for instance the interaction between the pipe and the bending stiffener (BS) at the BS-tip.

It was shown that the BS was too stiff in the local model, this resulted in an abrupt curvature response at the BS-tip. M2 suffered the most to this to this. The fatigue response in M3 was more jagged along the riser than the response in M2. A comparison of M3 with a more refined mesh was conducted. This did not give the desired improvement. The jaggedness could be understood from nature of the shear interaction model in ITCODE0, whereas ITCODE31 uses elementary beam theory after the moment-curvature relationship has been calculated.

The M3 model showed a pronounced hotspot damage in the root, which was believed being caused by the forced displacement the BS exerted on the pipe seeing that both the pipe and the BS were modeled in the same nodal system. This was tried solved with a contact model, M3X, where the BS and the pipe were modeled in independent nodal systems with the contact element, CONT130. M3X proved itself difficult to converge. In the end a separate load history was applied to M3X and in addition to M3 to demonstrate this load history also had the same tendencies as witnessed earlier. It was confirmed that the element type ITCODE0 has the same issues for a dependent and an independent nodal system, and it was therefore concluded that this element model must be revised in the future if it should be applied in similar fatigue assessments.

The use of hang-off angle and full representation of the BS paves the way for a less conservative fatigue assessment than the stub model. The biggest damage found along the length of the BS is 51% less than what is predicted from the stub model. However, it must be noted that the too stiff BS could have lead to less motion over its length since the pipe will get a hinge-like transition over the BS-tip for the upper threshold of wave responses. Even so, it is reasonable to believe that result for a correctly modeled BS will still give a lower estimated damage than what is found in the stub model. The conclusion is that the hang-off angle approach together with the ITCODE31 element is an interesting path to pursue. In addition, the stub model approach could always be conducted as a supporting model because of its fast solution time. As such, the already established method does not necessarily need to be abandoned.

Sammendrag

Abstract in Norwegian

Denne oppgaven benyttet ulike metoder for å modellere og beregne utmatting som følge av bølgelaster i strekkarmeringen på et fleksiblt stigerør i bøyestiverområdet. Målet med oppgaven var samtidig å gi leseren en grunnleggende forståelse av fleksible rør og stigerør samt den nødvendige teori for å gjennomføre en dynamisk analyse ved bruk av elementmetoden, og å beregne utmattingsskade fra irregulære tiddserier.

Det eksisterer ulike metodologier for å gjøre utmattingsanalyser på stigerør. Den generelle tilnærmingen er å benytte bevegelsesmønsteret fra en global stigerørsmodell, og å påføre dette mønsteret på en lokalmodell som har en mer nøyaktig representasjon av rørets tverrsnitt. I selve beregningen av utmatting benyttes SN-kurve og Miner sum. Variasjon av metoder omfatter hvordan modellene er laget, hva slags type laster som påføres globalmodellen og hvordan resultatene av denne blir overført til lokalmodellen.

Situasjonen var en ny feltutbyggelse nær Enchova feltet i Campos Bassenget utenfor kysten av Rio De Janeiro. Dette feltet skulle bli bygget ut ved hjelp av en *dreietårnforankret flytende enhet* med en *lat-bølget stigerørs konfigurasjon* på et 125 meter vanndyp. Dette ble modellert i RIFLEX ved simple rørformede elementer gitt med bøyestivheten til røret ved slipp. En irregulær bølgeanalyse med fel-

tets bølgedata ble utført.

Pagodemetoden (Regnfallsmetoden), ble anvendt for telling av de globale tidsseriene. De regulære spektrene fra denne tellingen ble delt i 40 binger. Tre forskjellige lokalmodeller ble laget i BFLEX. Den første modellen, M1, var en representasjon av rørets tverrsnitt, et avkapp, som ble påført de største kurvaturer og strekkverdiene funnet i bøyestiverområdet. Dette er en kjent modell i industrien. De to siste modellene var fullmodeller av bøyestiveren som ble påført en aksiell og en lateral last ved dekomponering av strekket med endevinkelen fra globalanalysen. Denne tilnærmingen er mindre anvendt. De to sistnevnte endevinkelmodellene benytter seg av to ulike formuleringer for modelleringen av strekkarmeringen.

M2 og M3 har vist seg å gi et mindre konservativt utmattingsresultat enn M1. Det kan forstås at M2 og M3 gir en mer realistisk representasjon av lastmønstret. De fanger også opp andre effekter, som for eksempel interaksjonen ved tuppen av bøyestiver.

Det viste seg at bøyestiveren ble for stiv i lokalmodellen slik at det ble et høyt kurvaturutslag ved tuppen. M2 var modellen som gav mest utslag på dette. M3 sin utmattingsrespons var mye mer volatil langs stigerøret enn hva som var tilfelle i M2. Det ble gjort sammenligninger med dobbelt så fin elementinndeling uten at responsen ble noe jevnere fordelt. Dette kan ha utløp i at M3 benytter en kontinuerlig interaksjonsmodell for trådene og røret som baserer seg på et virtuelt skjærkraftlag, mens M2 benytter alminnelig bjelketeori etter at moment-kurvatur kurven har blitt beregnet.

Det ble også kartlagt dannelse av heteflekker i M3 som følge av tvunget bevegelse i ståltrådene nær roten. Sistnevnte ble forsøkt løst ved hjelp av en kontaktmodell, M3X, hvor bøyestiver og rør ble modellert i to uavhengige nodesystem. En slik modell viste seg veldig vanskelig å få til å konvergere. Til slutt ble en separat analyse med en alternativ lasthistorie påsatt M3 og M3X, som viste at elementene benyttet i M3 har en endeeffekt, som må sees nærmere på om elementet skal benyttes til lignende lastmodeller i fremtiden.

Bruken av endevinkel og en full representasjon av bøyestiveren muliggjør et mindre konservativt anslag for levetiden enn avkappmodellen. M2 har 51% mindre utmattingsskade over bøyestiveren enn hva avkappmodellen fikk. Den altfor store bøyestiveren kan ha sørget for mindre bevegelse over bøyestiveren enn hva som er naturlig siden røret vil bevege seg som et hengsel over bøyestivertuppen for de største bølgeresponsene. Likevel er det naturlig å tro at resultatet for en riktig modellert bøyestiver fortsatt vil gi en anslått levetid høyere enn avkappmodellen. Konklusjonen er at M2 virker som en interessant metode å forfølge videre. En fordel er at en avkappmodell alltid kan kjøres ved siden av på grunn av dens kjappe løsningstid, dermed må man ikke forlate en allerede etablert metode med noe nytt.

Contents

List of Figures

List of Tables

Nomenclature

Roman Symbols

A	The cross-section of the beam $[mm^2]$ – eq 3.3
a	Initial crack length $[m]$ – eq 4.6
A_c	The external area taken with the outer steel radius $[mm^2]$ – sec 3.3.1
A_i	Area of internal cross-section $[mm^2]$ – 3.1
ds	Incremental curvlinear distance $[mm^2]$ – eq 4.5
EA	Axial stiffness $[N]$
EI	The bending stiffness $[Nmm^2]$
G	The shear modulus $G = \frac{E}{2(1+v)}$ $[MPa]$
GT	The torsional stiffness $[\frac{Nmm^2}{rad}]$
H_i	The vessel's transfer function. $H_3 = \frac{\eta_3}{\xi_a}[\frac{m}{m}]$ and $H_5 = \frac{\eta_5}{k\xi_a}[\frac{rad}{radm}]$
K	The stress intensity factor $[MPam^{.5}]$ – eq 4.6
k	In wave theory – k is the wave number. $k = \frac{2\pi}{\lambda}[\frac{rad}{m}]$
k	Shear stiffness $k = \frac{Gb}{t}[MPa]$– eq 4.5

m	The power constant in Paris' law $[-]$
P	External loading $[N]$ – eq 4.5
P_e	The hydrostatic pressure $[MPa]$
P_o	The operational pressure $[MPa]$
q_3	The pressure on the interfaces $[\frac{MPa}{m}]$ – eq 4.5
R^D	Damping force vector $[N]$ or $[Nmm^2]$ – section 4.3
R^E	External force vector $[N]$ or $[Nmm^2]$ – section 4.3
R^I	Inertia force vector $[N]$ or $[Nmm^2]$ – section 4.3
R^S	Internal structural reaction force vector $[N]$ or $[Nmm^2]$ – section 4.3
H_s	Wave theory – The significant wave height is the average wave height of one-third of the spectrum's highest waves. $[m]$
$S(\omega)$	The spectral density function $[m^2 s]$
T_p	Wave theory – The spectral peak period the period where the function has its maximum value $[s]$
T_z	Wave theory – The zero-up-crossing period is the average period between two up-crossings of the mean sea level. $[s]$
T_{eff}	The effective tension - top tension subtracted the buoyancy of the pipe $[N]$
T_w	The tensile force which the tensile layers have to endure $[N]$ – sec 3.3.1
v_s	Tendon displacement following Navier's hypothesis after bending deformation $[mm^2]$ – eq 4.5
v_p	Actual longitudinal displacement along the tendon $[mm^2]$ – eq 4.5

y	The distance from center of cross-section ymax is equal to radius $[mm]$ – eq 3.3
E	The Young's modulus $[MPa]$

Greek Symbols

α	Thermal expansion coefficient $[-]$ – 3.2
β_{2c}	Critical curvature for slip in the cross section $[\frac{1}{m}]$
ϵ	The strain, elongation of the specimen $\epsilon = \frac{\Delta L}{L}[-]$
ϵ	Wave theory – ϵ is a random value between 0 and π used by RIFLEX to create irregular waves $[rad]$
ϵ_M	Mechanical strain $[-]$ – eq 3.2
ϵ_P	Pressure strain $[-]$ – eq 3.2
ϵ_T	Temperature strain $[-]$ – eq 3.2
η_3	Motion in heave $\sum_{n=1}^{N} \sqrt{2S(\omega)\Delta\omega} H_3(\omega) \sin(\omega t + \theta_3 + \epsilon_n)[m]$
η_5	Motion in pitch $\sum_{n=1}^{N} k\sqrt{2S(\omega)\Delta\omega} H_5(\omega) \sin(\omega t + \theta_5 + \epsilon_n)[rad]$
γ	Wave theory – The constant that indicates the peakedness, the concentration of the spectrum around T_p. $\gamma = 1$ reduces the spectral function to a Pierson-Moskowitz spectrum.
θ_i	The phase angle between vessel and wave motion for heave and roll $[rad]$
κ	$\kappa = \frac{1}{\rho}$ The curvature $[\frac{1}{m}]$
μ	The linear friction coefficient between two materials $[-]$
ρ	$\rho = \frac{1}{\kappa}$ The bending radius $[m]$
σ_y	The yield stress of the material $[MPa]$

σ_{xx}	The stress distribution from axial loading $[MPa]$ – eq 3.3
ν	The poisson ratio $[-]$
ξ_{An}	The Wave amplitude. It is related to the spectrum as $\xi_{An} = \sqrt{2S(\omega)\Delta\omega}[m]$

Definitions

F_f	The fill factor $[-]$ – is defined as the relation between the breadth of each wire tendon multiplied with number of tendons divided by the circumference of the cross section times the cosine of the lay angle. As such the fill factor is a factor to decompose tendon area for the axial direction. The effective cross-section area is the nominal area multiplied with the fill factor, and analogously the effective axial stiffness can be found. $F_{f_i} = \frac{n_i b}{2\pi r \cos\alpha}$
α	The lay angle $[deg]$ – is the angle the tendon has to the longitudinal axis. If the lay angle is 90 degrees, the tendon is laid completely radial and if zero degrees it follows the pipe longitudinally. The pressure armor is close to 90 degrees to take the radial forces while the tensile armor is closer to 30 degrees to be able to take the tensile forces, but still be helical enough to take up torsional forces.
L_p	The pitch length $[m]$ is defined as the longitudinal distance which is passed for the tendon to spin one turn around the longitudinal axis. This is dependent on the lay-angle and the breadth of the tendon.

Acronyms

BS	Bending Stiffener
DFF	Design Fatigue Factor – from a risk matrix based on uncertainty and consequence the DFF is established. The fatigue analysis must clear the desired lifetime multiplied with the DFF.

EPC	Engineering, Procurement and Construction – In an EPC contract the supplier will deliver a complete product to the buyer. That is to say he will do the design based on customer requirements, get the material needed and build it.
FBG	Fiber Bragg Grating - A principle of calculating the difference in temperature/strain by analyzing the shifting wavelength of a transmitted spectrum from a special fiber sensor which is exposed to intense periodic UV light.
FEM	Finite Element Method
MBR	Minimum Bend Radius ρ_{min} for the pipe. It varies for operation and storage conditions.
TDP	The touch down point - where the pipe touches the seabed during installation.
UTS	Ultimate Tensile Strength
WL	Water Line for calm sea

1 | Introduction

The topic of this thesis is fatigue assessment of the tensile armor in the bending stiffener area. The goal of this thesis is to do a qualitative comparison of the fatigue response for three different local models that utilize data from the same global model. The author will make use of RIFLEX to model the global riser system and BFLEX for the local models.

Additionally, the thesis will present all the necessary stages to get to the point where such fatigue assessment can take place. The scope of the thesis also comprises a literature study. With that, it is the thesis' aim to give the reader an overview of the complete field associated with flexible pipes, risers systems and the modeling and lifetime predictions of such.

Offshore pipes are divided into flexible or rigid pipes; both have their area of application. In chapter 2 the flexible pipe will be presented along with its application in risers. This chapter will additionally give an overview of the first adoption of flexible pipes for the transport of hydrocarbons, the use of flexibles today, pipe design codes, the market players. Finally, a general outline of full scale testing and installation procedures will be presented.

Chapter 3 will present the mechanical behavior of flexible pipes, nonlinear effects, the stick-slip effect and pipe soil interaction. Additionally, an geometrical model for the stick-slip behavior is presented along with a comparison between the analytically derived pipe characteristics and the values provided by the pipe manufacturer.

The stepping stone for chapter 4 is the finite element method (FEM). This chapter will present the highlight of the applied theory in this study from that point of departure. It will briefly go through the use and capabilities of RIFLEX and BFLEX. Furthermore the two bending theories for tendons used in the BFLEX package will be presented. The principals of how BFLEX estimates fatigue life will be thoroughly reviewed here.

Chapter 5 is the start of the actual study. This part should be possible to read separately of those who are versed in the topics of BFLEX and riser fatigue. Chapter 6 will subsequently present the results of the study, while 7 is purposed for the discussion of the findings. Chapter 8 contains the conclusive remarks of the study while 9 presents the author's ideas for further work on the subject.

All data input is provided by KOGT Subsea if not specified otherwise. All element values are taken at end 1. Tension is always positive. Calculations are done in radians, but may be presented in degrees. Stress is given in MPa if not specified otherwise. Curvature κ is always given as $\frac{1}{m}$.

2 | Flexible pipe

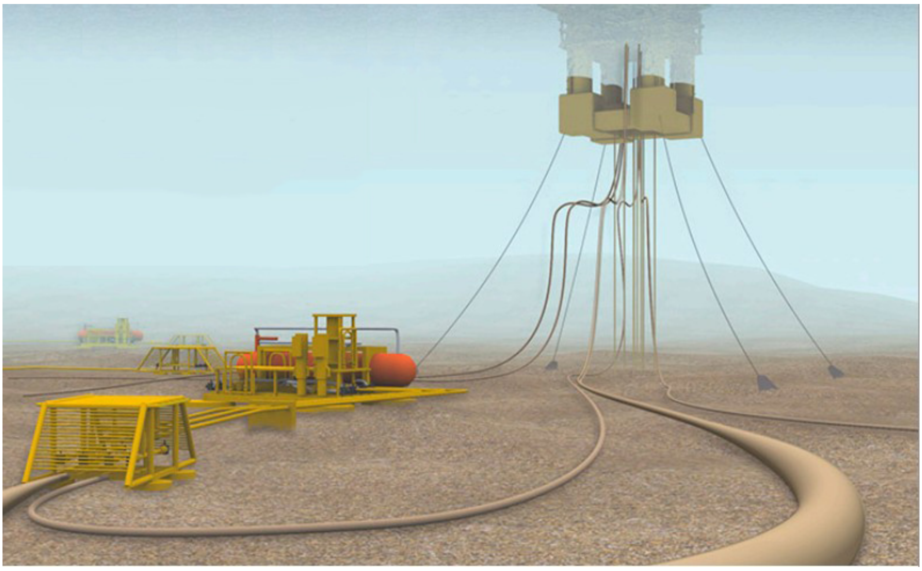

Figure 2.1: Different offshore applications of flexible pipes. Courtesy of Kongsberg

2.1 Introduction

A flexible pipe has a multi layered cross-section where the layers are either *bonded* by vulcanization or *unbounded*, the latter being where the layers are allowed to slide only subject to friction. In comparison to a rigid steel pipe they are characterized with low bending stiffness (EI), medium axial tensile stiffness (EA) and susceptible to pressure variations. The fundamental concept is helically wound metal layers together with a polymer sealing. This will is elaborated in section 2.2.

Offshore flexible pipes are used in the transport of hydrocarbons or condensate, for injection of water, gas or downhole chemicals. Additionally, flexible pipes can be used as control lines transporting control fluids, communication and electricity. These types of cables are referred to as *umbilicals*. Hydrocarbons can be *exported* subsea from a field to a receiving terminal onshore, these are called export pipelines. A notable example of the latter is the $44''$ Langeled rigid pipeline. (Gassco).

Flexible pipes normally have an internal diameter in the range of 2 to 20 inches and can be used for both static and dynamic designs.

In static design one can find the seabed flowlines and jumper cables. The reasons for using flexibles in static design are for instance when:

- it would have been more costly to prepare the route for rigid pipe with regard to free-spans.
- because the route requires steep curvature around existing installations.
- because the seabed has large gross movements i.e mudslide.
- because subsea installations or flowline location will change during the lifetime.

- it is desired to reuse the pipe on other projects after field life.

Flexibles are practical in *dynamic designs* because of their compliance to motion. They are used as offloading lines between buoys and vessels and in riser configuration from seabed up to floating units.

Another chief difference that characterizes flexibles is the contact layer between the bore and the transported fluid. The *roughbore* has a corrugated metallic carcass as the inner layer, which is suitable for a range of applications both topside and subsea. The steel carcass is an important part of the structural integrity of the pipe, when the carcass is lined with a polymer layer it is called a *smoothbore*. The smoothbore is a more expensive solution, which is used to combat pressure drop, erosion (Palmer [2008]) and pipe whistling (Crome [2007]), where the last-mentioned is a phenomenon which occurs in dry-gas under high pressure.

2.2 Composition

The figure 2.2 gives a representation of a typical non-bonded roughbore flexible pipe. Every layer has a given task.

The inner **carcass** (**1**) is an interlocked metallic layer that resists collapse from hydrostatic pressure and pressure from gas build-up in the annulus, which results from diffusion of hydrocarbons through the polymer sheaths in to the annulus – the void in the tubing. Different steel grades from carbon steel to nickel-based alloys can be used; the requirement comes from the composition, temperature and pressure of the product that will flow through it and especially in regard to corrosion from hydrogen sulfide (sour service). This is a weighted decision between several parameters because higher corrosion resistant alloys usually have higher temperature sensibility in yield stress, which in turn demands thicker pipe walls to take up the same pressure. At the same time these

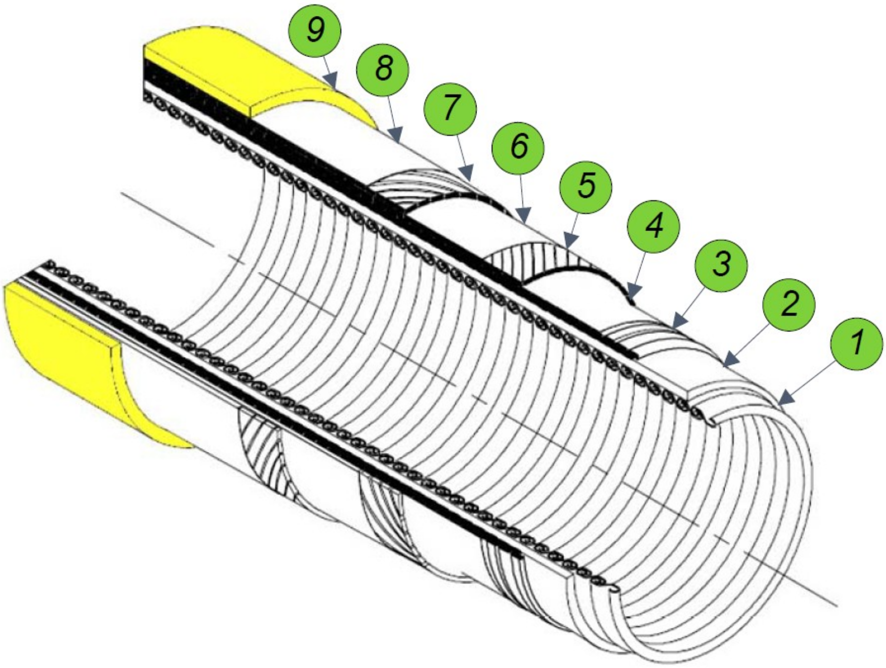

Figure 2.2: The layer composition for an unbounded flexible. Source Zhang [2003]

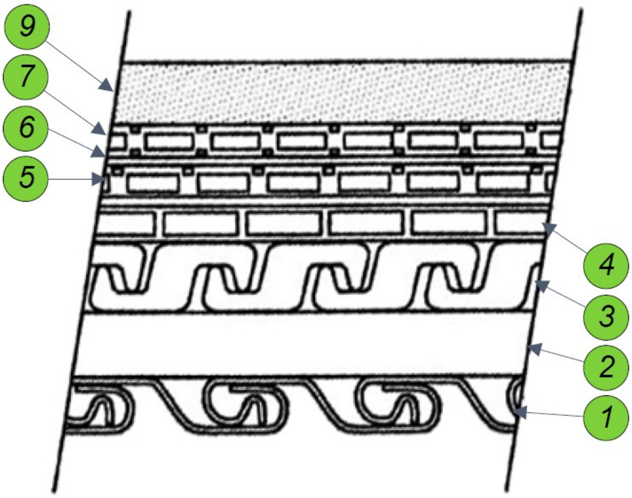

Figure 2.3: The layer's different cross-sections profiles. This figure is not showing the birdcaging tape. Source ISO [2007]

alloys are more expensive.

The **fluid barrier** (**2**) is a polymer sheath to maintain the fluid integrity of the pipe, which is extruded over the carcass.

The **pressure armor** (**3**) is usually also an interlocked profile, whose function is to withstand the hoop stress. In figure 2.3 a Z-shape profile is shown. The profile may vary, variations are shown in figure 7 on page 17 in ISO [2007]. The pressure armor is spun helically over the polymer sheath very close to 90° to the longitudinal axis for best absorbing the radial forces. There are various design considerations, but in general the material is a type of carbon steel. For high pressure application, a secondary pressure armor can be counter wound over this first one. The secondary pressure armor is seldom interlocked.

The **tensile armor** (**5 & 7**) resists the tensile load on the pipe and is normally spun at ±20° - ±60° on the longitudinal axis, they are counter wound to give resistance for both positive and negative torsional forces. The lower range of lay angles is used when a pressure armor is used. In some designs where the radial pressure is small, the pressure armor can be left out and the tensile armor is then spun at 55°, which is the torsional neutral lay angle. The tendons in the tensile layer has always a rectangular profile, but their breadth and height might vary from pipe to pipe.

The **anti-wear layers** (**4 & 6**) are anti-friction tapes to ensure that the wires do not get dragged out of their position by avoiding metallic contact and thus excelling the bending characteristic. The tapes are often a type of polyamid (nylon).

The combination of low tension or even compression and torsion can result in a failure mode named, quite figuratively, *birdcaging*, where the wire strands get twisted out of place. The **anti-birdcaging tapes** (**8**) are wound outside the outer tensile layer to keep strands from bulging. High modulus aramid or similar synthetic fibers are commonly used for this purpose. There are additional intermediate polyester layers of marix and diolen spread through the cross-section. These are bedding tapes to help keep the different layers in place during fabrication.

The **outer sheath** (**9**) prevents intrusion of seawater and mechanical damage throughout service life. For topside applications the outer sheath can be reinforced with an external carcass and fire resistant layers.

The structural design requirements are set to satisfy the pressure and temperature conditions from both the transported fluid and the external environment. For example, if needed, one can have an *insulation layer*, a secondary layer of cross wound tensile armor or as already mentioned; an extra layer of pressure armor. The use of better materials and extra reinforcement layers have to be considered to their cost-benefit – a pipe does not necessarily need to last for hundreds of years. A good lifetime prediction can optimize the design and give reduction in capital expenses. However, it is important to always be on the conservative side. Unplanned riser intervention still bears a stiffer pricetag than that of a more expensive design.

2.3 Failure modes

The pipe's layers can fail in numerous ways, but if one looks at the pipe as a whole, it has 8 ways to end its operational life prematurely. It can **burst** or **collapse**, and it can fail by **tensile**, **bending** and **torsional** forces. The lifetime can additionally be reduced by **erosion**, **corrosion** and **fatigue**.

Collapse is a failure mechanism where the carcass or pressure armor fails because of external pressure, or because the pipe is submitted to tension in an extent that the these layers become so elongated that they loose their ability to carry load hence collapse. If the pipe was already a bit ovalized from the installation collapse, this can happen quite unexpected. **Burst**, to the contrary, is fracture in hoop direction of the pressure armor as a consequence of excess internal pressure.

Tensile failure is damage or fracturing of the tendons in the tensile layer. This can be caused by too much tension which can typical happen during installation. Another reason can be that the layers have been weakened from wear to the extent that they can no longer sustain its operational conditions. Compressive forces can lead to **over-bending** which in turn could lead to ovalization and collapse, crack initiation or rupture in the plastic sheaths and unlocking of the interlocked pressure armor. **Torsional failure** is rare in operation, but over-twisting can lead to birdcaging or collapse of carcass and pressure armor. The pipe is more likely to suffer from over-bending and over-twisting during installation, and it is generally a problem close to the termination ends.

Erosion and **corrosion** are critical for the internal part of the carcass. This corrosion can be a problem for the other layers because it can lead to an increase in diffusion of fluid through the cross-section, hence increase the possibility of additional corrosion in the other layers.

Fatigue is an important element in all parts of the riser which have cyclic loading. Cyclic loading can come from pressure variations for the pressure armor along the pipe and the curvature variations in the section around the *hog bend* and the *bending stiffener* area. This project will address the issues of fatigue in the tensile armor in the bending stiffener area.

2.4 Bending stiffener

At the hang-off point, the transition between a riser and the platform's rigid piping can cause over-bending. Two different principals can be applied to keep the curvature and moment within the design limitations: the *bending stiffener* and the *bell mouth*. These designs are illustrated in figure 2.4. The bell mouth is a steel component with a curved surface which will protect against over-bending by not allowing the pipe to exceed the curvature of this surface, whereas the bending stiffener is a tapered structure made of polyurethane elastomer which will increase the overall bending stiffness of the riser. For riser applications the bending stiffener is often a separate structure which encloses the pipe with a small clearance. It is braced to a steel collar fastened to the rig which ensures the transfer of forces. In this project such a bending stiffener was chosen. The modeling of the bending stiffener is explained in section 5.3.2.

2.5 Buoyancy modules

The chosen design configuration in this project is the lazy-wave which is illustrated in figure 2.5. The intention of this form is to decouple the motions of the vessel from the subsea installation. Buoyancy and sometimes weight modules are added along the pipe to achieve this form.

A typical module is shown in figure 2.6. The buoyancy modules are made of syntactic foam and coated to avoid water ingress. They are clamped on the pipe. It is important to have a clamp which keeps the module in place while not damaging the external sheath of the riser. It was not necessary to model discrete modules along the riser in this project, and in section 5.3.1 it is explained which approach was done to get the lazy-wave shape on the riser. It can be noted that some water ingress is unavoidable, hence a decrease of buoyancy in the modules through the system's lifetime must be considered.

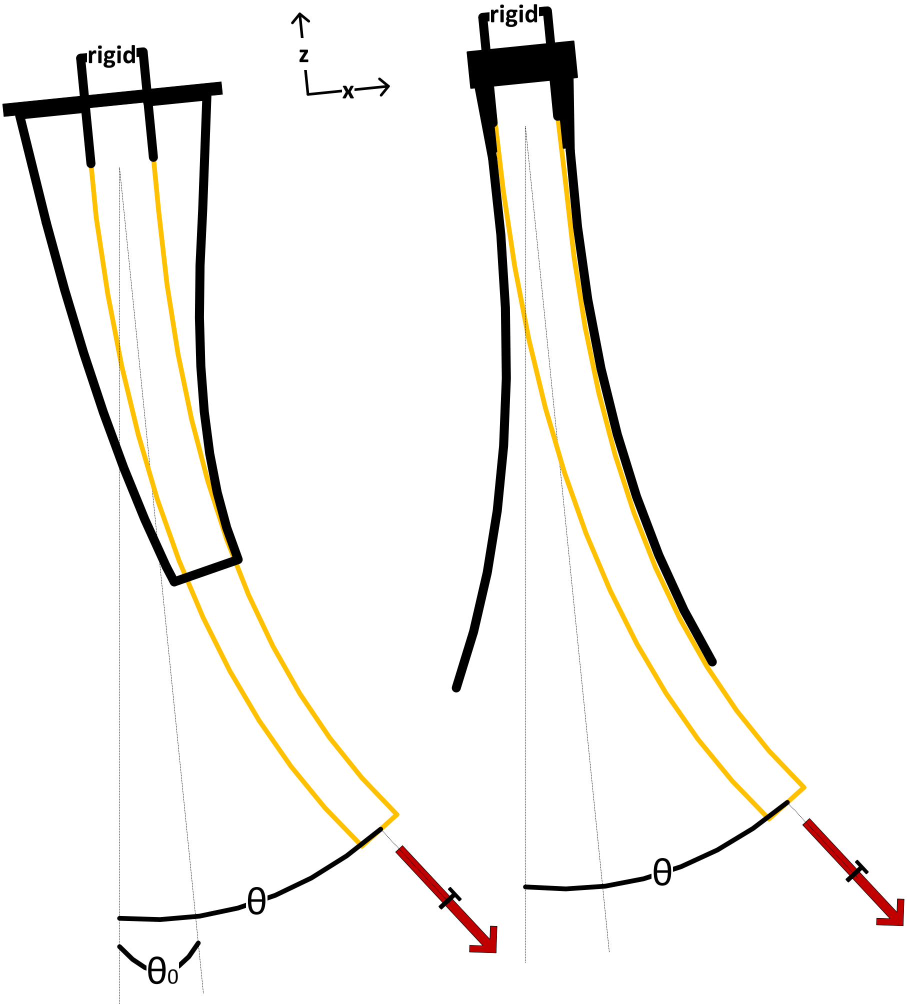

Figure 2.4: The principal overview of the bending stiffener (left) and the bell mouth design. θ is called the end-angle or hang-off angle. $\theta_0 = 8°$ is the static offset of the system or $\beta_0 = 82°$ off the x-axis. The whole system, which connects the rigid pipe to the BS and the BS to the rig, is called the *hang-off arrangement*

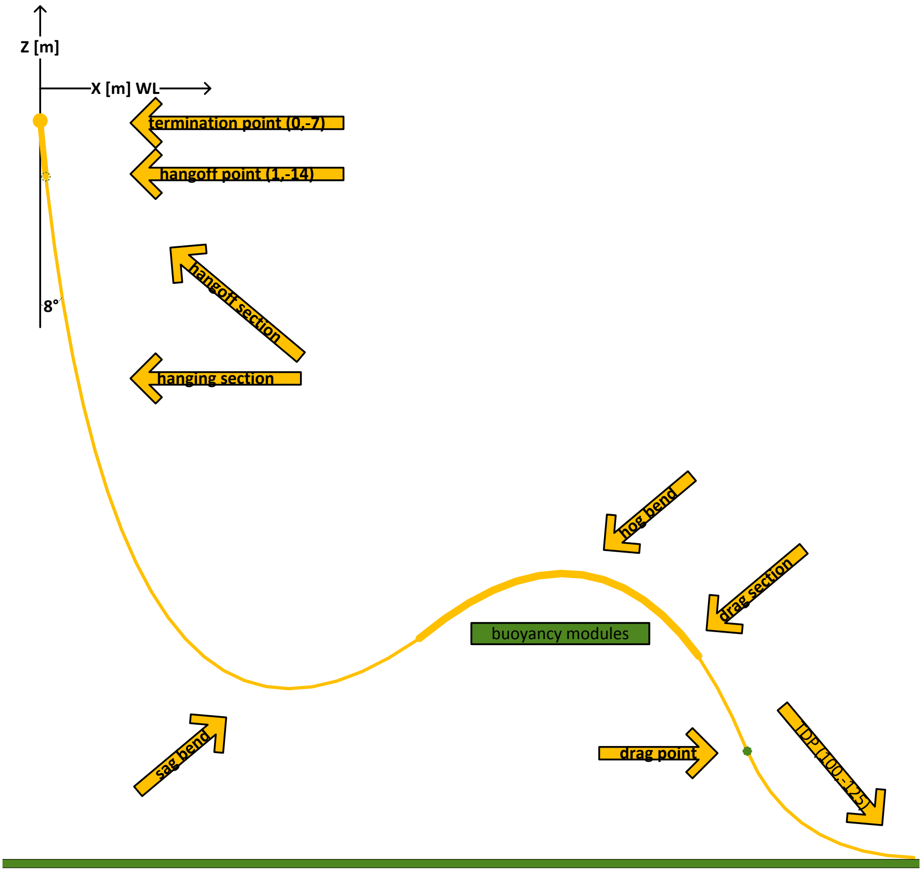

Figure 2.5: The intended lazy-wave configuration in this project with description of the different sections. *The hang off arrangement* is everything from rigid pipe to end of BS. The hang-off point is defined as point where the pipe exits the BS. Drag point is where the curve inverses. The coordinates are the actual ones, and the model starts at the top.

Figure 2.6: A close-up of the hog bend and the attachable buoyancy modules. Courtesy of Trelleborg.

2.6 Early look at flexible pipes

The first use of flexible pipes was during the Second World War during Operation PLUTO, *Pipe-Lines Under The Ocean.* Which were pipes, whose goal was to secure the fuel supply for the Allied Forces in Europe, they went under the English Channel from England to France and were continuously extended along with the troop movement to stretch forth to the Rhine. (TMB) The first flexible flowline in the North Sea was introduced in 1974 on the Beryl field then operated by ExxonMobil's subsidiary Mobil North Sea (Technip).

Although the basic concept has not changed since the 40's, flexibles undergo various types of degradation and can exhibit a wide array of failure modes; collapse, burst, tensile failure, compressive failure, over-bending, torsional failure, fatigue, erosion, corrosion, excessive wear from bad design or vibration and damage from external impact. Quite naturally, there has been substantial advancement in the knowledge and the ways to address these failure modes and to conform to the necessary operational conditions of today.

2.7 Flexibles in service

Today there are over 3300 offshore flexible pipes in service which accumulate almost 39 thousand years of operation. 90% of flexibles have an internal diameter less than 10 inches, 70% are used with design temperatures less than 80 degrees Celsius. 58% of these flexibles are seabed-to-surface pipes or *risers*. Of all risers, 70% are employed in waters with a depth less than 1000 meter and almost 50% are located offshore of Brazil. (Kenny [2010]). In 2007, there were about 200 flexible risers off the coast of Norway (**?**), and this number is increasing. In addition to numerous flow line applications, new fields such as Goliat and Johan Castberg will add more flexible piping to the continental shelf (Offshore.no).

2.8 Market players

The well-known flexible pipe manufactures for offshore applications are Technip, Wellstream and NKT Flexibles. Technip is in the lead with its three facilities; FlexiBras, FlexiFrance and lastly AsiaFlex, which is located in Malaysia. It is common practice that the pipe manufactures deliver on EPC contracts (**?**).

The producers of bending stiffeners and buoyancy modules are often multidisciplined like *Trelleborg Offshore* and *Balmoral Offshore Engineering* which design and manufacture an array of different riser ancillary devices, but there exist companies like *Floation Technologies* which solely focuses on one segment. Trelleborg has however the majority market share in the offshore buoyancy segment which was further strengthened on the 11th of April this year by the acquisition of Ambler Technology which is a world-renowned manufacturer of syntactic foam used in such modules (Trelleborg).

There is a small supplier diversity in this market. This is substantiated by the argument that flexibles pipes and subsea ancillary devices are expensive products which require high reliability, and that successful products rely heavily on experience and proprietary technology. Moreover the manufacturing of flexible pipes demands expensive production facilities.

2.9 Design and riser management codes

The American Petroleum Institute (API) is the primary author of the governing standards and *recommended practices* (RP's) for design, fabrication, installation and operation of flexible pipes. There exist ISO specifications based on these design codes. Furthermore the companies involved in manufacture, installation and operation may have their own derivations of the practices and regulations.

- API RP 17B, Recommended Practice for Flexible Pipe fourth edition (ISO 13628-11:2007)
- API 17J, Specification for unbounded Flexible Pipe third edition. (ISO 13628-2:2006)

Additionally *Det Norske Veritas* (DNV) has several RP's for both steel and flexible risers and pipelines amongst them two noteworthy ones are:

- DNV-RP-F206, Recommended Practice for Riser Integrity Management
- DNV-RP-F204, Recommended Practice for Riser Fatigue

2.10 Performance analysis by full-scale testing

It is required to do full-scale testing and verifications of all new designs, thus such testing is not a segment which is perishing with the advancement of computers. MarinTek, *the Norwegian Marine Technology Research Institute* which is housed in the very same facilities as the *Department of Marine Technology* has a full-scale testing bench to do dynamic tests of risers with BS or bell mouth.

MarinTek is eager to expand this area with a larger testing facility (Sævik). The guidelines for full-scale *dynamic fatigue tests* are given in section 9.7.2 in ISO [2007]. Both element types which will be used in this thesis have been studied and compared against full-scale models (Sævik [2013]).

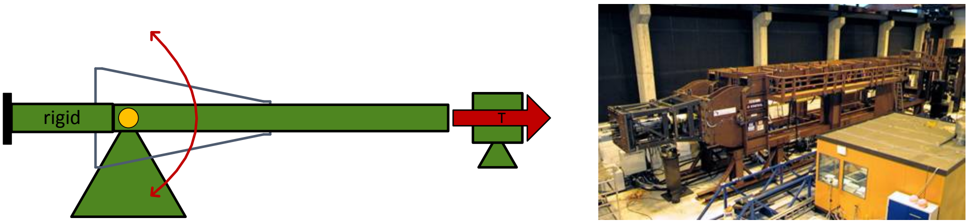

(a) An illustrative sketch

(b) Overview photo

Figure 2.7: In the testing bench at MarinTek, the sample pipe and BS are fastened to a rigid connection and suspended on a rocker arm whose pivot point is located a distance in on the BS. A type of winch is connected to the pipe end to give the system tension.

2.11 Installation procedures

Flexible subsea piping and flexible risers can be installed from a range of different service vessels from specialized dynamic positioned pipelay vessels to simple barges moving on anchor. The shorter pipes can be coiled together and stored onboard directly, whereas the longer pipes would require *reels* or *carousels*. A typical reel can have an outer diameter of five to eleven meters. A criterion for the reel is that the internal diameter is not lower than the minimum bend radius – the MBR. It can be noted that reeled pipe can be designed to pass yield strength as lay vessels can have *straightening devices* to relieve the pipe for residual stresses as it is being reeled off.

For a reel lay vessel, one can find a *reel drive system* which can handle sev-

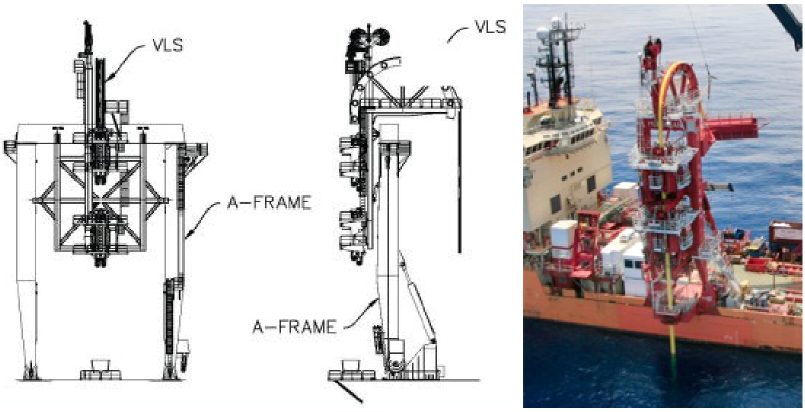

Figure 2.8: Vertical lay on DSV Toisa Proteus

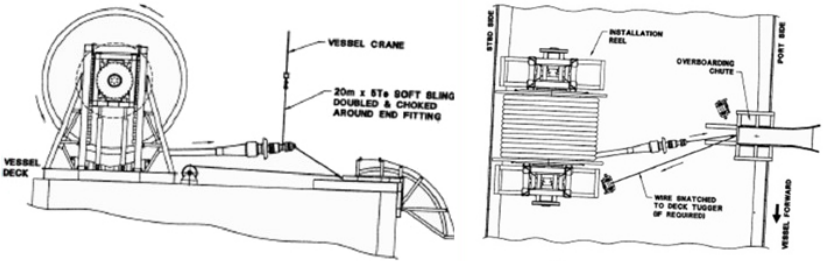

Figure 2.9: Schematic display off the reel overboard over a chute

eral reels, and feed them overboard on *a chute*, an illustration of this concept is seen in figure 2.9. Lay speed can be up to 800 meters per hour, the bottlenecks being ancillary equipment like buoyancy modules, bending stiffeners and intermediate connections. There exist other solutions, most notable are the vertical lay systems seen in figure 2.8.

For flexible pipes the installation part is crucial. over-bending while storing and handling the pipe can happen, and tools or sharp objects on board the vessel might damage the external sheath. When deploying the pipe in to the water it is important to supervise the lay tension and the curvature at exit. If using a chute, whose radius is too short or tension is too high, the pipe could ovalize as it is getting crushed against the chute. It can be hard to control these parameters for deep water installation, as such a vertical lay solution can be better suited. In vertical lay there are tensioner squeezes which secure the pipe, thus the pipe is only submitted to axial tension. This removes the risk of ovalization and increases the allowable lay tension (SUT [2012]).

3 | Mechanical behavior

Intrinsically a flexible has considerably lower bending stiffness than a rigid pipe. The plastic layers are the main contributors to bending stiffness after *slip* (ref. section 3.3). The Young's moduli of the plastics used in these pipes are highly dependent on temperature. The pipe applied in this project becomes 28.9% stiffer at 10° than it is at 20° Celsius. For the actual project where the pipe was originally employed the stated operational bending stiffness for low and high ambient temperature differs with nearly 50%

Furthermore, the axial stiffness (EA) is 3-4 times less than for a rigid pipe, while the *thermal expansion coefficient* (α) is of similar order. Analogously to mechanical strains, the axial elongation from *internal pressure* is equally increased. This is seen in equation 3.1 when considering the static equilibrium of a cutout of the cross-section. Here the tensile armor (A) needs to resist the pressure over the internal cross-section.

$$\sigma_P \cdot A = P_o \cdot \pi \frac{D_i^2}{4} \rightarrow \epsilon_P EA = P_o \cdot \pi \frac{D_i^2}{4} \rightarrow \epsilon_P = \frac{P_o}{EA} A_i \tag{3.1}$$

In linear theory the strain contributions are added together by summation. It is seen in equation 3.2 that strains from axial force and internal pressure are inversly proportional to the axial stiffness. Thereafter, the thermal strain becomes four times less prominent.

$$\epsilon_1 = \epsilon_T + \epsilon_M + \epsilon_P = \alpha \Delta T + \frac{1}{\frac{1}{4} EA_{steel}} \left(T + P_o A_i\right) = \alpha \Delta T + 4 \left(\frac{T + P_o A_i}{EA_{steel}} \right) \tag{3.2}$$

3.1 General nonlinearity

Because of the inhomogeneous cross section and large deflection, a flexible pipe will often be a nonlinear problem. Nonlinearity can be divided into *geometrical* and *material* nonlinearities.

Geometrical nonlinearities have to do with the kinematic relations of the displacements and rotations, and their lack of smallness. Non-conservative loads which are dependent on the specimen's deflection or a material stiffness which vary with deflection are also subjects here. For a cross-section of a multi-layered pipe there will exist complicated contact conditions on the boundaries of the layers. These contact conditions can also be classified as *nonlinear boundary* conditions.

Material nonlinearities are when the stress-strain or temperature-strain relations behave nonlinearly. Typical engineering materials can be divided into a pre-yield and post-yield phase, where yield is defined as a single point or a transition zone where the material loses its linear stress-strain behavior and start to harden, also known as *cold working.* For a flexible this can happen on the reel, which normally leads to some residual strains that need to be corrected with straightening devices before overboarding.

It is fairly straightforward to extend the theory to calculate the moment and curvature of a pipe using nonlinear material, using *equilibrium* (3.1b) and compatibility assumption (3.1a). The only condition is that the bending action has not lead to *ovalization* of the cross-section. One needs a flow rule and a relation between strain and curvature. The flow rule states the material's stress & strain before and after yield, whereas the relation between strain and curvature can commonly be assumed linear following *Navier's hypothesis*.

As such, one can predict the stress in the cross-section given a radius, say, from the inner diameter on a reel, and thus estimate the maximum residual strain when reeled. Steel and other engineering materials which are loaded past yield in to the elastoplastic area can in general be simplified by linear relations. For instance that the post-yield modulus is linearly related to the one for pre-yield, i.e $\tilde{E} = 0.15E$. The steel used in this project is defined in this way – see figure 5.1.

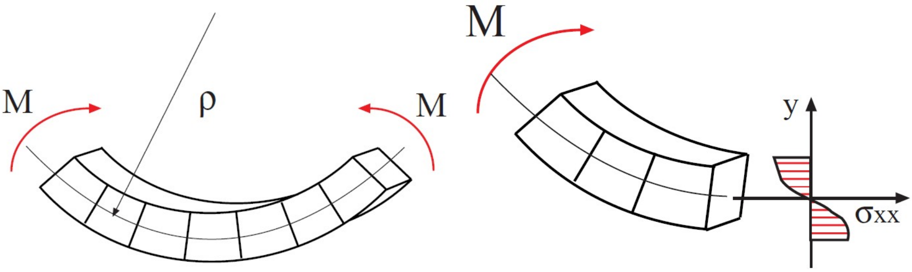

(a) Navier's hypothesis - Eq: 3.4 (b) Equilibrium of moment - Eq: 3.3

Figure 3.1: Laws independent of material behavior

$$\text{Equilibrium} \qquad M = \int_A \sigma_{xx} \cdot y \mathrm{d}A \tag{3.3}$$

$$\text{Compatibility} \qquad \epsilon_{xx} = -\frac{y}{\rho} \tag{3.4}$$

3.2 Pipe strength and stress components

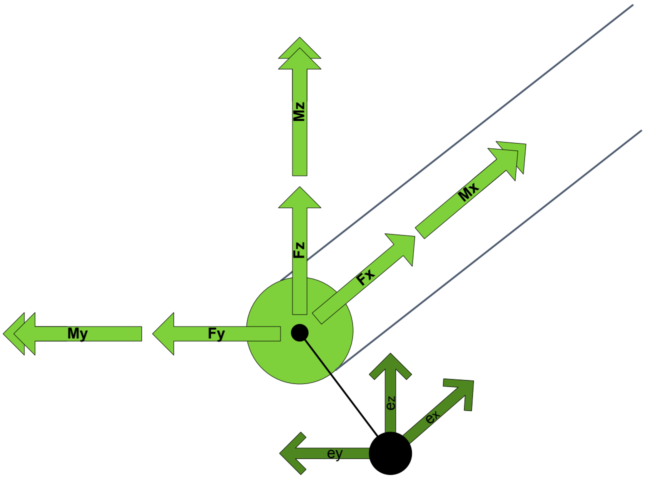

Figure 3.2: Load and nodal definition, pipe Sævik [2012b]

The different loads can be divided into axisymmetric, torsional and bending loads.

The plane *axisymmetric* loads come from the internal and the hydrostatic pressure, and can be divided into radial and hoop stresses. The pressure armor which is almost completely radial takes the largest part of the internal pressure, yet the tensile armor will contribute significantly. The carcass does not carry any part of the internal pressure.

Axial force is taken up by the tensile layer, which has a lay angle, α. A non-dimensional parameter named the *fill factor (F)* indicates the ability of each layer's ability to take up axial stresses and inversely to take up the radial stresses. Equation 3.5 can be used to calculate the axial stiffness. These analytical equations are elaborated further in Sævik [2012a]. The area is calculated using thin-walled area formulation, alternatively one can use the given tendon area times number of tendons. r_i is taken as the mean radius of each layer.

$$EA = E \sum_{i=1}^{2} 2\pi r_i F_i \cos^4(\alpha_i) \tag{3.5}$$

The flexural response in bending is a design issue for both operation and installation. A non-bonded multi-layered pipe has a hysteric bending behavior because of the *stick-slip effect*. As a rigid pipe, where the tendons do not slip, the bending stiffness can be estimated by the equation 3.6. This value is seldom given in the data sheet as normal practice is to neglect the stick-slip behavior and only use the bending stiffness for the pipe in slip.

$$EI = E \sum_{i=1}^{2} \pi r_i^3 F_i \cos^4(\alpha_i) \tag{3.6}$$

Torsional loads are small during normal operation, but can be an issue at the termination ends if installed improperly or during rough seas. The main contribution to torsional resistance comes from the tensile armor. The torsional strength can be estimated by tendons alone – equation 3.7. It assumes that the layers remain in contact.

Additionally tension will straighten the tendons thus counter torsional forces and help stiffen the pipe. Sævik [2012a] states that this effect of pipe stiffening is accounted for by checking that the torsional strength for a tensile force is not larger than the minimum axial force found by dynamic analysis.

$$GT = E \sum_{i=1}^{2} A_i r_i^2 \cos^2(\alpha_i) \sin^2(\alpha_i) \tag{3.7}$$

3.2.1 Comparison of the analytical formulas to the given values

EA and GT were given for the pipe (fig. 5.2). This is an opportunity to compare the analytical formulas given in section 3.2 to the values found in the data sheet. The area is taken as the given tendon area $- 2\pi r_i F_i \cos(\alpha_i) = a_i \cdot n_i$. Modulus for steel is set to $E = 200GPa$ and lay angles are found in layer description (fig. 5.3). It is seen in equation 3.8 that the analytical axial stiffness is nearly six percent larger than the the given one. From equation 3.9 it is found that the analytical torsional stiffness is almost ten percent lower. There are more contributers to torsional strength than the tensile armor alone, so it is no surprise that the analytical formula which only accounts for the tensile tendons underestimates the strength. The axial stiffness in the data sheet is probably calculated with a more precise modulus. The range of modulus for steel is generally between 180 and 200 GPa and the uncertainty falls within these boundaries.

$$90E \cdot \big(44\cos^3(0.5515) + 46\cos^3(-0.555)\big) = 998[MN] \tag{3.8}$$

$$\begin{aligned} 90E \cdot \big(44 \cdot 133.8\cos(0.5515)\sin^2(0.5515) + 46 \cdot 140.8\cos(-0.555)\sin^2(-0.555)\big) \\ = 119[\frac{kNm^2}{deg}] \end{aligned} \tag{3.9}$$

3.3 Stick-slip effect

The layers are free to move only subjected to friction. For small curvatures the shear force on the tensile layer is less than the available friction. When the tendons in the tensile layers are restrained by friction to move the layer acts as a rigid part. Then the tendons will pivot around the pipe's neutral axis as a solid structure as formulated by the *parallel axis theorem* (*Steiner's theorem*). As such, before *slip* the tensile armor contributes with a much larger bending stiffness than the contribution from the plastic layers.

When submitted to excess bending the shear force overcomes the available friction of the tendons and they will start to *slip*. The Steiner contribution will disappear when the wires starts to slide. From then on the bending stiffness will only have contribution from the plastic sheaths and the individual wires in the tensile layers around their proper axis, which is much lower.

The wire will slip both transversely and longitudinally towards the *geodesic*, the shortest distance in the cylinder plane, see figure 3.3. The critical curvature, β_c, where slip occurs, is defined where the shear force equals the resisting friction force.

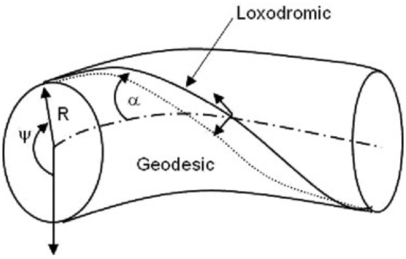

Figure 3.3: The definition of curve paths. The loxodromic curve is the initial path of each steel wire, whereas the geodesic represents a straight line in the cylinder plane.

From classical bending theory it is known that the shear is at its maximum at $r = 0$. The steel layers will start to slip where the shear is at its maximum, at the neutral axis. In addition the outermost layer will sense larger frictional forces, because of larger contact pressure resulting from the seawater column. Moreover, the slip angle on each side of the layer will be slightly different. Sævik [2012a] states that this difference in curvature is small enough to model the slip as an instantaneous event. For a pipe with two layers of tensile armor there will exist two critical curvatures, one for slip of each one; β_{2c1} and β_{2c2}.

Figure 3.4 demonstrates a typical M/κ relation of an unbounded flexible pipe with two steel layers together with the total contribution from the plastic layers. The combination results in a trilinear curve.

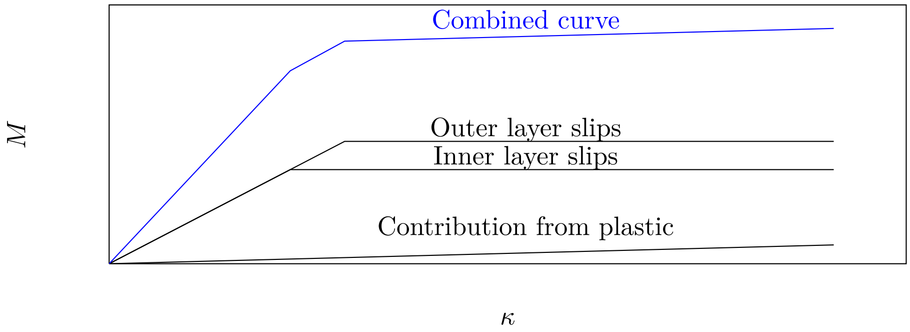

Figure 3.4: The total contribution from two layers steel layers and the plastic layers.

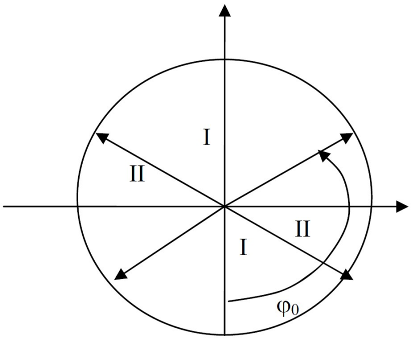

Figure 3.5: I - the stick region and II - the slip region for one tensile layer. A pipe with two layers will have two slip angles. The slip angle is given in eq. 3.11

The slip curvature can be expressed as an equation, 3.10. Its relation with the critical angle is given in equation 3.11. This is an analytical expression which assumes no end-effects, constant interface pressure, equal friction coefficients for static and dynamic situation and no interaction between the tendons themselves. Further reading of this theory can be reviewed in Sævik [2012a].

$$\beta_{2c} = \frac{\mu(q_3^I + q_3^{I+1})}{EA\cos^2\alpha\sin\alpha} \tag{3.10}$$

$$\varphi_0 = \cos^{-1}\left(\frac{\beta_{2c}}{\beta_2}\right) + \frac{\pi}{2} \tag{3.11}$$

3.3.1 Calculate slip by an analytical model

The interface pressure q_3 in equation 3.10 can be calculated by geometrical considerations. To give an example, one can assume that the pipe's moment-curvature curve at TDP during installation is desired. The water depth is set to 650 meters. Here the hydrostatic pressure is assumed to be much larger than the tensile force, so the interface pressure is given by the hydrostatic pressure alone.

$$T_w = T_{eff} - P_c A_c \tag{3.12}$$

$$T_{eff} << P_c A_c$$

Furthermore it can be assumed that the hydrostatic pressure from the water column is in its *entirety* taken up by the tensile armors, and that internal pressure is neglected for simplification. It is noted that the plastic does not take up pressure, i.e. the pressure derivative over the thickness is equal to zero. The interface pressures can then be derived by geometrical approach. With no effect from the plastic layer, the interface pressures from the two layers will equal: $q_{3_1}^{I+1} = q_{3_2}^{I} = \frac{p_c}{2}$, $q_{3_1}^{I} = 0$ and $q_{3_1}^{I+1} = p_c$.

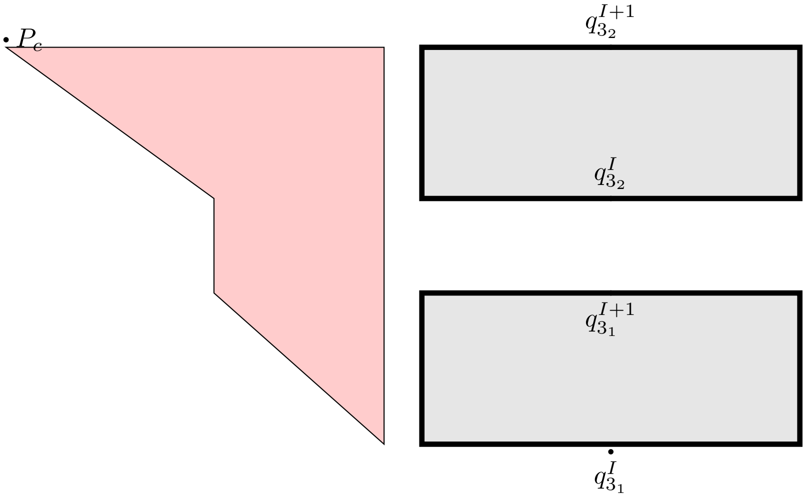

Figure 3.6: Simplified model to illustrate the interface pressure. Hydrostatic pressure, p_c, distributed in its entirety over the tensile armor. No internal pressure.

The friction coefficient used in equation 3.10 is set to $\mu = 0.3$. By calculation the slip curvatures are found to be $\beta_{c_1} = 1.27 \cdot 10^{-4}$ and $\beta_{c_2} = 3.30 \cdot 10^{-4}$. Thus low slip curvature on the innermost layer. The moment is then calculated up to first slip and then to second slip with elastic theory; $M = EI\kappa$. The bending stiffness used in the plot is found in table 5.3.

These critical points are plotted together with the contribution from the plastic layer in figure 3.7. This serves only as a simplified model. It must be noted that the slip curvature will vary for pressure – higher pressure gives higher slip curvature as the shear resistance will be higher, hence the slip values are

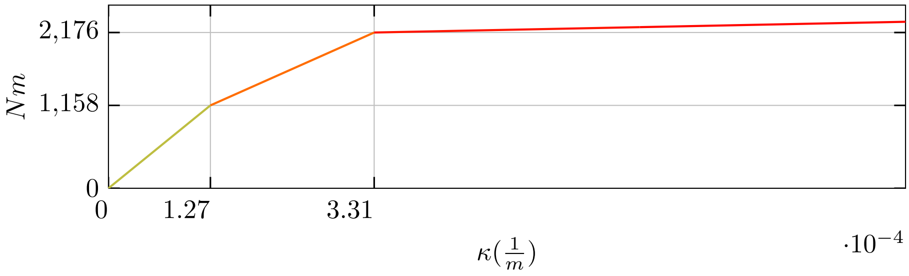

Figure 3.7: Plot of the net moment-curvature relation for an example case for the pipe.

different at TDP and at bending stiffener. In BFLEX only parts of the riser is studied in one model. For the pipeline installation software SIMLA the stick-slip effect can be included and studied for instance at TDP with the pipe element COMPIPE42 which allows for custom axial, bending and torsion curves. In this way one can study the effect in a whole riser model without the detailed cross-section of BFLEX.

3.4 Interaction between soil and pipe

The interaction between soil and pipe is clearly a key for on-bottom stability and buckling analysis, but also relevant for the installation procedure. Using nodal springs to model the contact surface is an effective constraint for pipeline models in FEM because the pipe can then be free to move as it naturally would. This can reveal pipe snaking and upheaval buckling. The possible downward displacement can result in an underestimation of the curvature at TDP, if the seafloor is modeled as a rigid contact surface.

In figure 3.8a one can see a pipe cross section which has penetrated the ocean floor. Intuitively one can think that the soil can give in substantially after contact, that the pipe digs into the loose soil, but after some distance will meet an nearly impenetrable wall. The interaction between the soil and the pipe can, for this application, be described as non-linear springs which are soft in the start and after a given displacement become too stiff to allow for any further movement. An illustration of this is demonstrated in 3.8b, where the x-axis is vertical displacement (η_3) downwards through the soil, and the y represents the corresponding force ($k_3 \cdot \eta_3$). If the model requires it, lateral (η_2) and axial (η_1) friction can be modeled in a similar fashion with linear springs. This can be relevant for pipeline analyses after installation.

In order to obtain the spring stiffness, a geological survey is ordered over the designated area of interest. Here one can establish the contour plot of the seabed and through seismic data establish a model for the hardness versus depth in the layered sand and clay of the seabed. If no survey exists *KOGT* uses $\mu_1 = 0.4$ and $\mu_2 = 0.5$ for rocky seabed and $\mu_1 = 0.175$ and $\mu_2 = 0.7$ for muddy. The higher lateral resistance in mud is based on partial submersion in to the soil (Kirkvik [2013]). *DNV-RP-F110* presents analytical formulas for estimating downward resistance and weight of an overburden of mud or rock in the case of trenching.

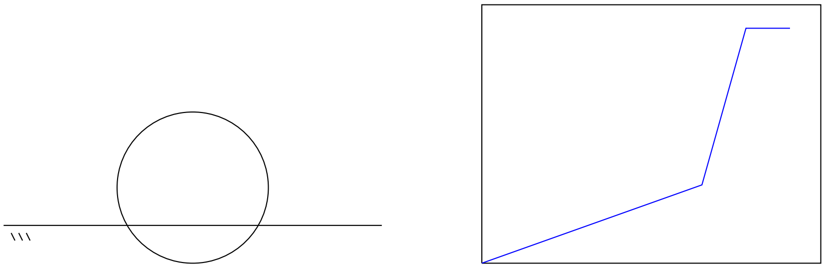

(a) Pipe surface penetration

(b) How k_3 increases w/ displacement

Figure 3.8: A soil – pipe interaction model.

4 | Applied theory

RIFLEX is a program used to do global analysis of flexible risers, but its use can also be extended to mooring lines, fish cage systems, pipelines and steel catenary risers. In this thesis, RIFLEX was used to do a nonlinear irregular global analysis of a riser at a water depth of 125 meter.

BFLEX is a tool used to do detailed cross-sectional analysis of fatigue and extreme loads. It uses much of the same syntax as SIMLA, but whereas SIMLA is limited to thin walled tubular cross-section, BFLEX can model the correct cross-section such as the carcass, pressure and tensile layers. As such it includes a bending formulation for tendons and is able to look at the rather intricate interaction between the different layers. BFLEX is as such not suited for global analysis, but rather for analysis in close proximity of the termination end. In this project three models were established in this program. One so-called *stub* model which is made up of 2 elements and two full-sized models of the bending stiffener where the two different beam formulations were applied; The Sandwich Beam Formulation (SBM) and the Moment Formulation (MM) respectively.

This chapter will serve as a highlight of the theory applied in this project.

4.1 Stress and strain measure

Slender structures, such as pipelines, have small strains. As such it can be convenient to use strain and stress measures which relate to the undeformed element. The stress tensor named 2^{nd} Piola Kirchoff together with its energetic conjugate Green strain tensor are preferred. This stress tensor does not vary for rigid body motion, and it does only change when the material is deformed.

These strain and stress measures for an uniaxial case are given here to illustrate the difference to the regular ones used in linear problems:

$$\text{Green strain } \Delta E = \frac{L\Delta L}{L_o^2} \tag{4.1}$$

$$2^{nd}\text{PK stress } S_{11} = \frac{L_0}{L}\frac{F}{A_o} \tag{4.2}$$

4.2 Total Lagrangian formulation

The FEM reference system applied in solid mechanics is normally described with the Lagrangian description of motions, which describes how points of the material deform. This is common for all analyses of solid structures. The contrary is the Eulerian description which describes a point in space, ideal for fluid motions. The nonlinear finite element formulation applied on pipe elements in programs like RIFLEX, Simla, BFLEX, Orcaflex and Usap is called the co-rotated total Lagrangian formulation (CTL).

In the total Lagrangian formulation, displacement is referred back to the initial undeformed configuration. By using the stress measure and strain tensor that were mentioned, the equilibrium equation will be defined with respect to the initial configuration.

4.2.1 Co-rotation

For flexible pipes, which undergo large displacement, the stiffness matrix and the equilibrium equation become elaborate, because the rotations are given relative to the inertial coordinate-system. A *co-rotated element* coordinate-system is introduced in each element. It follows the deformed nodal coordinates of the element as illustrated in 4.1. The rigid body motions are promptly omitted from the total motion of the nodes given in the inertial system, and only the relative translations and rotations are left. The relative displacement between the undeformed and co-rotated system is small, and by neglecting higher order terms of the strain tensor, there is no need of transformation when updating the strains and stresses. The global displacement, on the other hand, must be transformed before updating.

It is important to note that since the co-rotated frame is given by the nodal coordinates of the element, the elements must be small to ensure small relative rotations. Hence, the parts with large curvature should be modeled with a finer element grid than the part that will be lying on the seabed. In reference to figure 4.1, the axial strain can be directly computed by uniaxial Green Strain seen in equation 4.1, whilst bending deformation is calculated by measuring the relative deformation from the undeformed coordinate system and the co-rotated one.

By starting with the Total Lagrange equilibrium equation, introducing the Green strain and lastly the co-rotated reference system. The incremental equilibrium equation in Sævik [2012a] is given as:

$$\int_V \mathbf{C}_T : \Delta\epsilon : \delta\epsilon dV_0 + \int_V \sigma : \delta\Delta\mathbf{E} dV_0 - \int_s \Delta\mathbf{t} dS_0 = 0 \tag{4.3}$$

In equation 4.3 the $\mathbf{C}_T$ represents the tangential stiffness. The second term is known as the geometric stiffness matrix, which is proportional to the present stress with respect to a strain increment, $\Delta\mathbf{E}$. A schematic illustration on how the co-rotated total Lagrange can be implemented for a static analysis is presented in 7.5.5 in Sævik [2012a] for further reading.

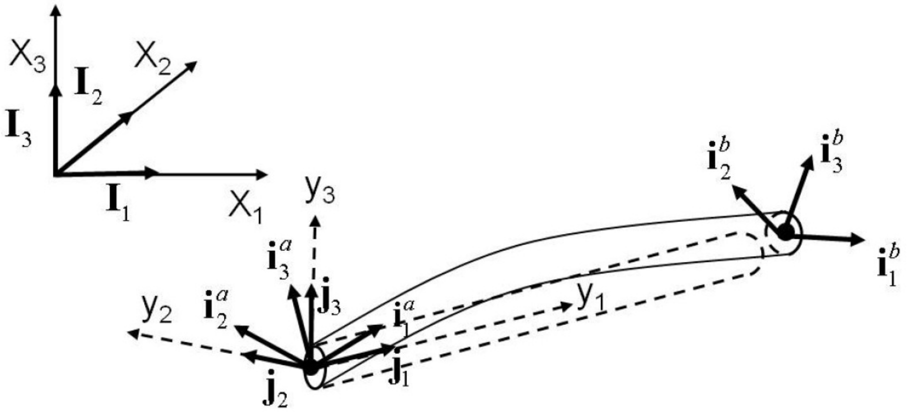

Figure 4.1: 3D beam element in CL formulation. The element reference system $\mathbf{j}_i$ is found by combing the tanget vector connecting the two nodes at the updated coordinate position with the current orientation of the element end node base vectors $\mathbf{i}_i^a$ and $\mathbf{i}_i^b$. Sævik [2012a]

4.3 Dynamic time domain analysis

$$R^I(r,\ddot{r},t) + R^D(r,\dot{r},t) + R^S(r,t) = R^E(r,\dot{r},t) \tag{4.4}$$

Dynamic equilibrium equations in RIFLEX and BFLEX are solved in the same manner as the static equations but they will include inertia and damping terms. The normal Newton-Rhapson (NR) iteration is applied in both RIFLEX and BFLEX, that is to say that the stiffness matrix ($\mathbf{C}$) is updated at each step. The convergence criteria used for dynamic analysis is similar to that of static convergence criteria, a value between 10^{-6} – 10^{-5}. This method has a second order convergence rate, however for big systems the generation and decomposing of $\mathbf{C}$ at each step can be time consuming. It can be established less frequently with only a small reduction in the convergence rate. This alternative, which is dubbed the *modified NP method* is not supported in RIFLEX, but is found in numerous FEM programs. In figure 4.2a the conventional method is illustrated, the measure of precision is based on the measured difference in displacement between two iterations. (Δr)

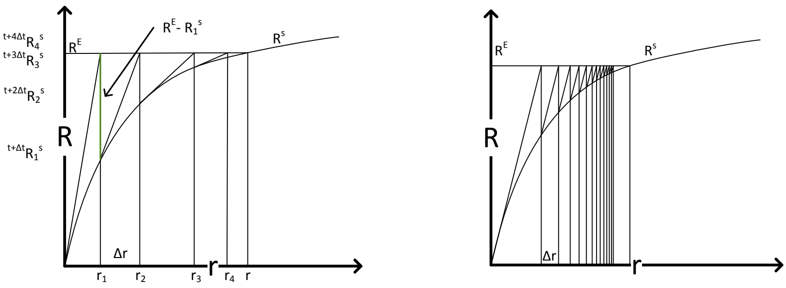

(a) Conventional – updating $\mathbf{C}$

(b) Modified – Not updating $\mathbf{C}$

Figure 4.2: 2D Illustrations of the two Newton-Rhapson's iteration methods.

In RIFLEX the mass matrix is set as concentrated. It is assumed that the damping is proportional to the strain velocity at each point, thereby making the damping proportional to the stiffness matrix alone. Thus a global proportional damping is applied with the mass damping coefficient $\alpha_1 = 0$ and the stiffness coefficient $\alpha_2 \geq 0$. A standard KOGT value for the latter is $\alpha_2 = 0.002$. The BFLEX models are in fact static problems for this project, however the setup of dynamic analysis is analogous to RIFLEX.

The dynamic response in both RIFLEX and BFLEX is calculated with direct time integration of the equation of motion (eq. 4.4). The method commonly used for nonlinear dynamics is the general Newmark integration. An example of Newmark integration is demonstrated in appendix C. The method is adjusted by the weight parameters β and γ. $\beta = \frac{1}{4}$ and $\gamma = \frac{1}{2}$ give the constant average acceleration time integration (*the trapezoidal rule*). This choice of weight parameters is unconditional stable i.e energy preserving for linear systems, and gives a second order accuracy. However, stability is *not always* preserved for nonlinear systems. Having a $\gamma > \frac{1}{2}$ will damp the solution, and filter out the higher modes, since damping grows with the $\frac{h}{T}$-ratio where h is the step size for the method. Damping of the solution is done to filter out false high-frequency vibrations which can arise from wave propagation (Ivar Langen [2010]), and does not degrade accuracy. Numerical damping also speeds up the convergence rate thus opens for bigger time steps. Standard KOGT values are used $\beta^{-1} = 3.9$ and $\gamma = 0.505$.

It is important to be aware of the *accuracy* of the algorithm. As long as the method is unconditional stable, the step size is the only concern for accuracy in time integration. In general terms, stability should not be a problem for a typical riser analysis. For the use of other weight parameters, the Wilson-θ parameter, $\theta \geq 1$, serves as an extension to the Newmark method by using time steps on the form $t + \theta\Delta t$ instead of $t + \Delta t$. This approach can be utilized to ensure that other methods of Newmark integration becomes unconditional stable, such as the linear acceleration method, $\beta = \frac{1}{6}$ and $\gamma = \frac{1}{2}$ for $\theta \geq 1.37$. RIFLEX includes the use of Wilson-θ which falls back to standard Newmark for its default value, $\theta = 1$. It should be noted that the use of Wilson-θ is known to have the tendency to overshoot the exact solution for nonlinear problems (Shuenn-Yih Chang).

4.4 Load model in RIFLEX

The loads on the system include weight, inertia, hydrostatic forces, hydrodynamic forces and the vessel induced motion. In the RIFLEX model the riser is clamped to the vessel. The vessel displacement and rotations are described as linear responses to the waves. The vessel's rotations are applied to the nonlinear riser system as prescribed rotations. The consistency between linear vessel motion and the co-rotated FE formulation is upheld by using the same convention for nodal rotations for the vessel as the nonlinear model. For further reading one can consult chapter five in the theory manual of RIFLEX.

4.5 Bending theory for tendons in BFLEX

Under elastic bending one can assume that the displacement between the initial curvepath and the geodesic is small – figure 3.3. Hence, for numerical stability, the transverse slip of the tensile armor is neglected in BFLEX. It is furthermore assumed that the cross-section keeps its form sufficiently to allow for analytical calculation of the local bending and torsion.

4.5.1 Sandwich beam formulation in BFLEX

Sandwich theory is in essence beam theory with multiple layers. The SBM in BFLEX considers the equilibrium equation of each tendon considering the shear interaction with the core pipe. As such this approach requires the helices to be explicitly mapped, and the tensile layers are given in polar coordinates. The formulation is numerically demanding, and the practical length these beams can have is limited.

SBM is formulated in terms of potential energy for each tendon. The algorithm calculates equilibrium of the entire cross-section at each load step. BFLEX has two solutions algorithms of this type: *ITCODE0* and *ITCODE1*. Whereas the latter calculates the slip value of each layer, the first one calculates only for the inner layer. The slip of both layers is then governed by the inner layer. Since the inner layer will be dominated by fatigue, i.e always more curvature and almost equal tension. The ITCODE0 is deemed as a good choice.

$$\prod = \frac{1}{2}\int_0^l EA\left(\frac{dv_s}{ds}\right)^2 + \frac{1}{2}k(v_s - v_p)^2 ds - Pv_p \tag{4.5}$$

Here v_p is the actual longitudinal displacement and v_s is the displacement following Navier's hypothesis. k is the nonlinear shear stiffness parameter that describes the stick-slip behavior. P is the external loading. The shear deformation γ in figure 4.3 is defined as $\gamma = \frac{v_s - v_p}{t}$ where t is the thickness over which the shear deformation occurs. The shear stiffness can promptly be written as $k = \frac{Gb}{t}$ where G is the shear modulus and b is the width of the beam.

4.5.2 Full moment formulation in BFLEX

In the moment formulation the pipe behavior and responses are established based on the friction between the layers. As such BFLEX calculates the bilinear moment/curvature relationship as illustrated in figure 3.4. The cross-section will have two regions as shown in figure 3.5; one stick and one slip. The bending stiffness from slip is given by the user as the cross-section data, while the stick is calculated by using the friction coefficient also supplied by the user. In this study the ITCODE31 algorithm will be used which calculates the moment-curvature curve for each layer. BFLEX's ITCODE21 uses the same approach however lets all layers have the curve from the inner layer.

Comparative studies have found that the full moment formulation gives less stress for extreme load cases than the SBM, however that it still gives the best

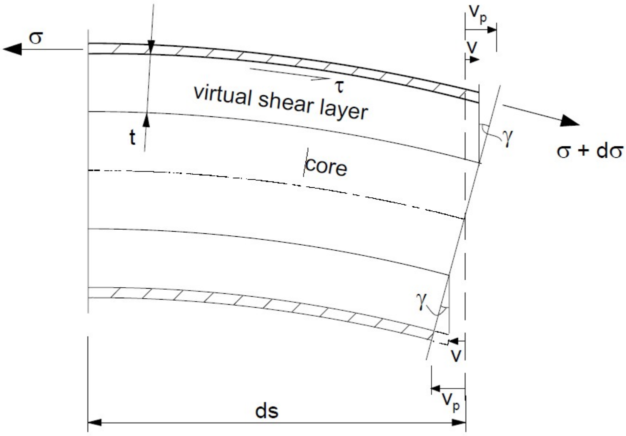

Figure 4.3: The SBM as illustrated in Sævik [2000]

fit when comparing against full scale fatigue test with FBG sensors (p36 Sævik [2013]). The full moment is a good way to model the slip mechanism in flexible pipes for fatigue purposes, requires less modeling than the SBM and is numerically faster.

4.6 Fatigue

Material failure of fatigue is where natural occurring minuscule cracks in the material grows because of repeated loading and unloading. Fatigue is the field of study which deals with damage and lifetime prediction of such loading.

Fatigue is first and foremost divided into *low-cycle* and *high-cycle* fatigue. Low-cycle fatigue is cyclic loading which comes close to yield or well in to the plastic range, whereas high cycle is loading which does not cause plastic deformation to the material. The characteristic span of high-cycle fatigue is 10^3 to 10^8. Above this regime one speaks of *very high cycle fatigue* where the stress-based approach to be presented in this project can fall too short for some materials.

4.6.1 SN-curves & Paris' law

SN-curve or Wöhler curve is the specimen's crack growth curve in terms of stress and cycles, and it is employed in high-cycle fatigue. It relates how many N constant cycles the specimen can withstand with a given *stress amplitude* – ΔS before it fails of sudden fracture. The theory extends to both nonlinear and linear crack growth behavior. The SN-curves used in offshore fatigue calculations are often linear or bi-linear. A bi-linear curve takes into account a slowdown of crack-growth at high cycles, say, over 10^7 cycles.

Tensile armor is made of flush steel with negligible initial crack (a). The *stress intensity factor* (K) is therefore equal to one. For such steel the majority of the fatigue life will be in the *crack initiation* phase, and not in the part where Paris' law (eq. 4.7) is valid. Nevertheless, the concept of a power relationship between a cyclic loading and *'crack growth'* is still applied to calculate the fatigue life. The linear SN-curve is analogous to *Paris' law* as seen in equation 4.8.

$$\Delta K = \sigma\sqrt{\pi a}F = 1 \tag{4.6}$$

$$\frac{da}{dN} = C\Delta K^m \tag{4.7}$$

$$\log\left(\frac{da}{dN}\right) = \log\left(C\Delta K^m\right) \longrightarrow \log\left(\frac{da}{dN}\right) = m \cdot \log(\Delta K) + \tilde{C} \tag{4.8}$$

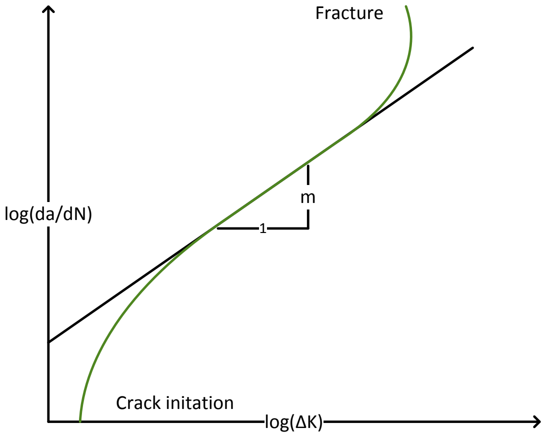

Figure 4.4: This graph shows the crack growth ratio over the stress intensity factor. The constant part with constant increment m is the true validity range for Paris' law.

Create a SN-curve

Data for SN-curves are typically gathered by running trials of simple bar elements in laboratory. With a given cycle-frequency and the desired stress the bar specimen is cycled to fracture. This marks a dot in the SN-chart (fig. 4.5). Several runs with the similar stress are undertaken to minimize measuring errors, and the trials will continue down to a reasonable low ΔS to complete the curve. The mean stress, *R-ratio* through the trials is kept constant (eq. 4.9). The SN-curve is only valid for one R-ratio as mean stress affects the fatigue life. It can also be noted that for tension wires it is desired to only cycle the stress on the tension side. The R-ratio is therefore in the range of 0.1-0.5 (Sævik).

$$R = \frac{\sigma_{min}}{\sigma_{max}} \tag{4.9}$$

The SN-curve is often taken as the median line through the data points and

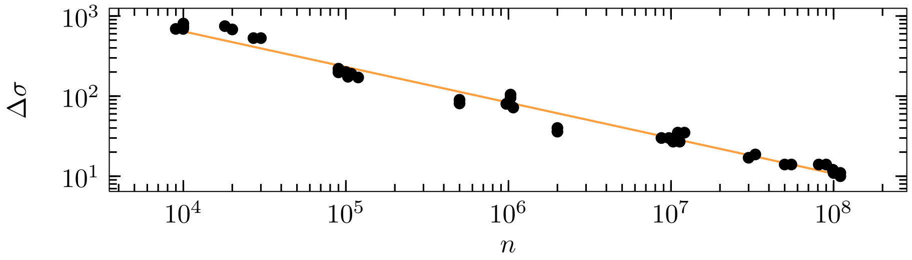

Figure 4.5: loglogplot of an example test specimen data and its fitted power curve

hence this line represents an expected failure of 50%. SN-curves used in design are usually more conservative than this since the median SN-curve is found in laboratory trials, therefore it can be shifted downward by one or two standard deviations of the dataset. Different industries use different guidelines and practices for establishing these curves, tough the principal remains the same.

4.6.2 Damage Rule – the Miner sum

The fundamental concept of lifetime prediction for general engineering is that each cycle contributes linearly to the total sum of damage. A set of cycles has a part-damage to the whole. This *damage rule* is dubbed after its inventors, *the Palmgren & Miner's Linear Damage hypothesis*, or short: *the Miner sum.* It is important to note that the damage rule does not look at the sequence of the loading nor takes account for residual stresses. The damage rule can only be used for bins of constant stress. An algorithm for cycle-counting is needed to transform irregular times series to sequences of constant stress.

$$D = \sum_i \frac{n_i}{N_i} \tag{4.10}$$

In equation 4.10, n_i is the number of cycles for a constant stress level while N_i is the calculated maximum number of cycles this stress level can sustain given the SN-curve. The normal definition is that $D = 1.0$ equals fracture.

4.6.3 Cycle-counting of irregular time series

The basis for applying the miner sum is a series of bins with constant stress. Broad-banded irregular time series have varying stress reversals about the mean-crossing as seen in figure 4.6. They need to be reduced to bins of constant stress. An algorithm for cycle-counting is needed. In fatigue design, it is wide consensus that the *Rainflow counting method* serves this purpose the best (C. Amzallag [1993]). The article from ASTM International is recommended for further reading about cycle counting procedures.

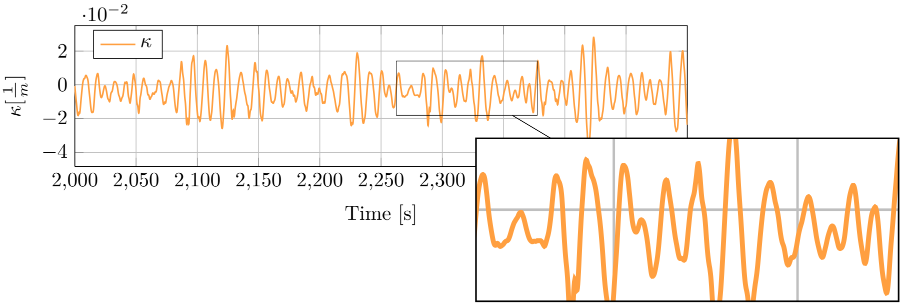

Figure 4.6: Excerpt of the time series for curvature from LC8 on an element corresponding to $x = 3[m]$

The cycle counting can be represented in a range spectrum as seen in figure 4.7. It may be directly used, and alt tough these are cases of constant stress it would still be an unsuitable number of load cases for BFLEX. The spectrum is divided into a given number of bins. In this illustration nine bins span the whole spectrum where the last bin is a zero range. Each bin will have an mean curvature and a curvature range.

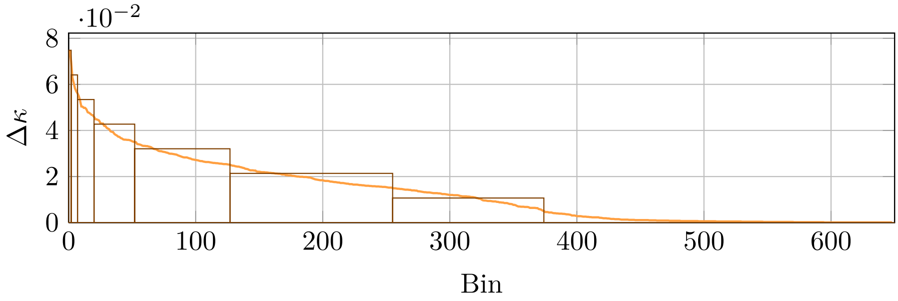

Figure 4.7: Cycle-Counting: This figure shows the *curvature range spectrum* from LC8 on an element corresponding to $x = 3[m]$. The spectrum is divided into 9 bins. Bin 1 and 2 are not dividable in this graph.

The Rainflow counting procedure applied in this project is provided by MarinTek and is based on the aforementioned article (C. Amzallag [1993]). The strength of their algorithm is that it has the possibility to count two or more sequences of different dimensions jointly. This is important since the model will need that the ranges of curvature & tension and hang-off angle & tension are actually coinciding. It uses a master/slave approach if the sequences are in conflict. The curvature and hang-off angle were chosen as masters. The range spectra were divided into 40 bins.

4.6.4 Mean stress effect

As mentioned one SN-curve is only valid for one R-ratio. This is because mean stress in cyclic loading contributes to an increase in fatigue damage even tough the $\Delta\sigma$ might be lower. One can not create SN-curves for every possible mean stress, hence it is necessary to transform a given SN-curve from one R-ratio to another. This is consequently called *mean stress correction.* The linear Goodman and the quadratic Gerber corrections are the most used. Testing of steel specimens confirms the reduced fatigue strength to be somewhere around these two corrections (Sævik). If the given SN curve was created at zero mean stress i.e $R = -1$ the Gerber and Goodman are given as in equation 4.8a.

$$\frac{\Delta\sigma}{\Delta\sigma_0} + \left(\frac{\sigma_m}{\sigma_u}\right)^2 = 1 \qquad (4.11)$$

$$\frac{\Delta\sigma}{\Delta\sigma_0} + \frac{\sigma_m}{\sigma_u} = 1 \qquad (4.12)$$

(a) σ_u is the UTS – $\Delta\sigma_0$ range in the given SN curve

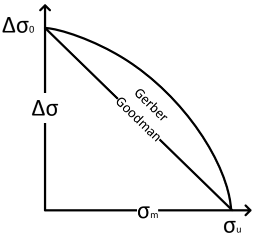

(b) Plotted together

Figure 4.8: The two common mean stress correction factors for SN curve at $R = -1$

One can express the stress range for a given R-ratio in terms of stress by combining $\sigma_m = \frac{\sigma_{max}+\sigma_{min}}{2}$ and $\Delta\sigma = \sigma_{max} - \sigma_{min}$ with the R-ratio. This leads to equation 4.13.

$$\Delta\sigma = 2\sigma_m \frac{1-R}{1+R} \rightarrow \sigma_m = \frac{1+R}{2(1-R)}\Delta\sigma \qquad (4.13)$$

Plugging 4.13 into either Gerber or Goodman gives the explicit correction to apply the given SN-curve for $R = -1$ for an arbitrary mean stress. For the Gerber equation this yields:

$$\Delta\sigma_0 = \frac{\Delta\sigma*}{1 - \left(\frac{\Delta\sigma*(1+R}{2\sigma_u(1-R)}\right)^2} \qquad (4.14)$$

$\Delta\sigma*$ is then the stress range to be used in the given SN curve to find the number of cycles to failure. This project applies the Gerber correction.. For the tensile armor, BFLEX calculates the correction given $\sigma_m = \sigma_{xx}$.

4.6.5 Uncertainty and safety factors

- A corrosive environment would affect the fatigue life significantly.
    - Diffusion of the transported fluid through the cross-section.
    - Puncturing of the external sheath and the subsequent intrusion of seawater in the annulus
- State of the art damage inspection *is not* complete albeit helps assess the most common situations which lead to reduced lifetime.
    - Top-side pressure check of the *annulus vent ports* to confirm or disprove annulus flooding.
    - *Line-going inspection* tools can measure the extent of seawater in the annulus, determine *outer* tensile armor wire thickness, scan for holes in the sheath and confirm damaged, disorganized and snapped tensile wires.
- The consequence of fatigue failure is global failure.

For these reasons the *design fatigue factor (DFF)* for riser systems is invariably ten. That is to say that if a lifetime of 25 years is desired, then the requirement of the analysis would be 250 years.

5 | Input & models

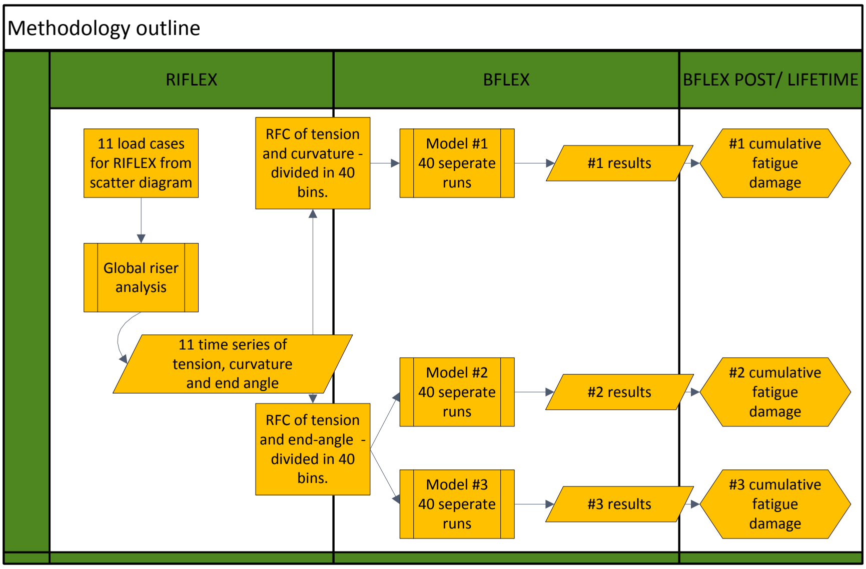

Table 5.1: The general outline of the different stages in this study. The desired parameters, hang-off angle & tension and curvature & tension, from the 11 sea states are Rainflow counted and combined in two separate paired range spectra which are divided into 40 blocks each.

5.1 Mechanical properties for the pipe

The project will apply a 8″ production riser for sour-service from NKT flexibles. The author has been given a design report from the aforementioned riser which originally was meant for two fields in the Congo offshore sector. NKT states that the operational depth range of this particular riser is 542 to 663 meters. Regardless, it is proposed that this design is sufficient for this task, since the governing design would not differ much. The cross section is made up of two tensile armor layers.

Symbol	Value	Unit	Description
D_i	203.2	mm	Inner diameter
D_o	478	mm	Outer diameter
M_d	241	$\frac{kg}{m}$	Dry weight
M_s	56.1	$\frac{kg}{m}$	Submerged weight
EI_p	227.3	kNm^2	In slip at operation and low ambient temp
EI_s	8905	kNm^2	In stick
EA	940.3	MN	Axial stiffness
GT	131.4	$\frac{kNm^2}{deg}$	Torsional stiffness
T_c	5.391	MN	Damaging pull – yield in tensile layers
P_o	21.4	MPa	Operation pressure
MBR_o	4.65	m	Minimum bending radius during operation

Table 5.2: The characteristic properties of the pipe.

5.1.1 Layer description for the pipe

5.3 presents the cross section description used in BFLEX. The tape layer given after the two tensile layers is actually between these two layers. The carcass was modeled with a profile, which was provided in the BFLEX example files and scaled to this pipe's layer thickness.

Carcass	C203_3247	$t = 10$mm
α	87.8	deg
Tape layer	Low modulus	$t = 0.8mm$
Plastic layer	Polyamid	$t = 9mm$
E	320	MPa
Pressure layer	Steel	$t = 8mm$
A	76.18	mm^2
Tensile layers	Rectangular	$t_i = 6mm$
n_i	44 / 46	-
A_i	90	mm^2
F_i	0.92	-
α_i	31.6 / -31.8	deg
p_i	1367 / 1427	mm
EI_i	4132 / 4773	kNm^2
Tape layer	Low modulus	$t = 1mm$
Plastic layer	Polyamid	$t = 12.8mm$
E	320	MPa
Insulation layer	Elastic material	$t = 82.4mm$
E	52.25	MPa

Table 5.3: The layer description for the pipe cross section.

The bending stiffness contribution from the tensile layers in stick is calculated per layer according to equation 3.6. The moduli for the plastic layers were not given, so they were given characteristic values. The insulation layer's modulus was adjusted in such a way that the bending stiffness in slip for the pipe became equal to EI_p. It must be emphasized that EI_p is not given as an input to BFLEX, but is calculated given the layer description found in table 5.3.

5.1.2 Properties of the steel in tensile armor

Because of confidentiality, the stress & strain and SN curve are not from the actual steel used in the pipe but given as relevant steel properties one will find in this type of steel. Prof. Sævik provided these properties to the author.

Stress & strain curve

Trilinear-steel is used in the tensile armor and is given by the curve in figure 5.1, otherwise elastic steel with $E = 200\text{GPa}$ and $\nu = 0.3$ is applied.

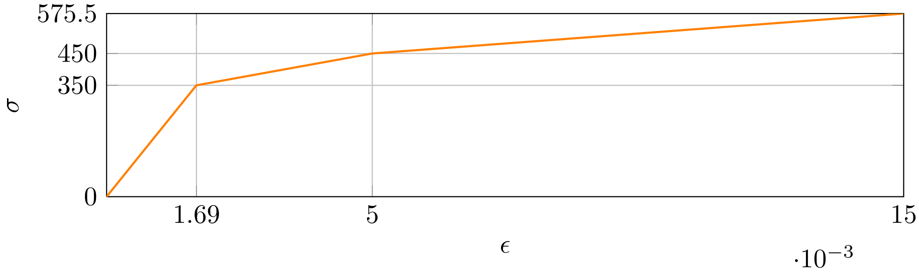

Figure 5.1: plot of the trilinear steel used in the tensile armor.

SN curve

This is a high strength steel with a $\sigma_{uts} = 1030MPa$.

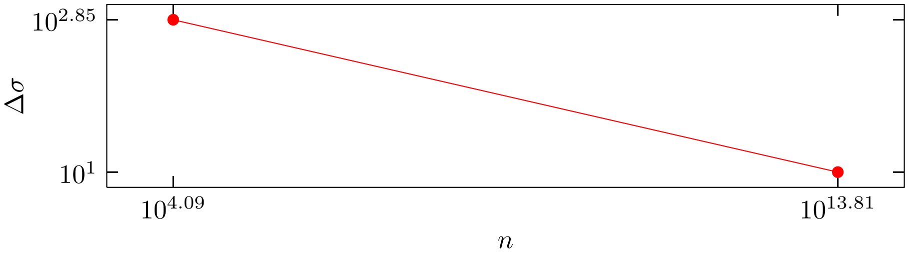

Figure 5.2: loglogplot of the SN curve used for the tensile armor

5.2 Establish the fatigue load cases

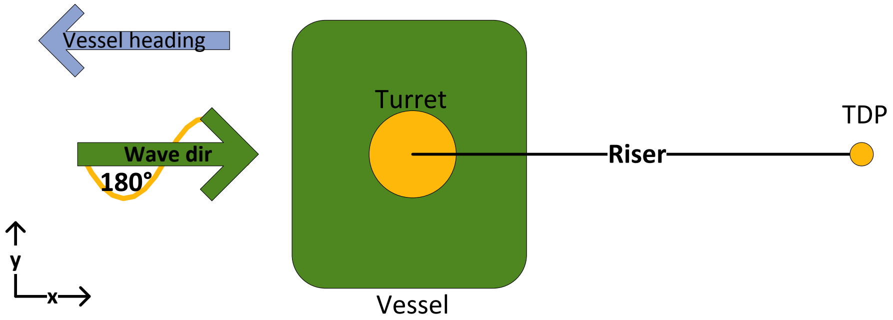

Figure 5.3: The wave direction definition for this project. No offset. No current.

A turret moored vessel distinguishes itself by being able to *weathervane*. It will passively or by thrusters orient itself to the most favorable position in respect to wind, current and waves. Using thrusters to orient itself is particularly important for shipshape vessels to avoid beam sea that can excite large roll motion.

Load cases are commonly set up with the use of an omni-directional wave spectrum with different headings. A separate *vessel-heading analysis* could give the probabilities of the vessel's orientation over a year. Table B2 in DNV [2011] is the offshore standard if no other data is known. It states that one should conduct the fatigue analysis with a weighting that 180° head sea has 60% probability of occurring. ±15° has 30% and ±30° has 10% probability of occurring.

In this project only head sea will be considered to lessen the number of load cases.

5.2.1 Scenario

The location of this project is close to the Enchova field located in the Campos Basin off the coast of Rio De Janeiro, Brazil. The very same which in 1977 was the first field to go into production in the Basin. The reservoirs are found in depths ranging from 100 to 130 meters. This field will be developed with a *turret moored floating unit* with *lazy-wave configuration* at a water depth of 125 meters.

5.2.2 Response amplitude operator - RAO

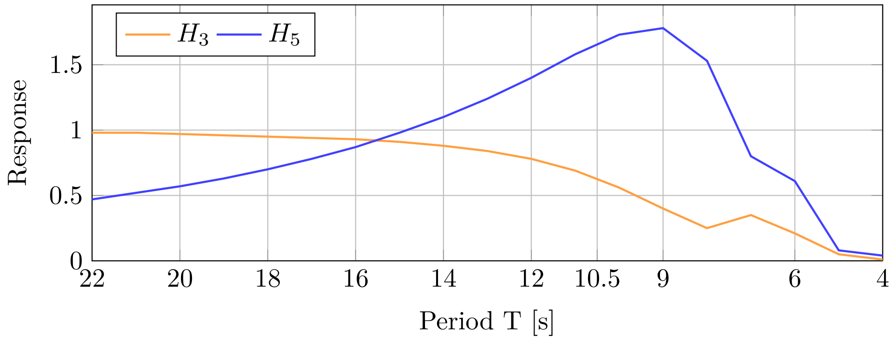

Figure 5.4: The RAO for pitch and heave - head sea (180°)

A single response amplitude operator is given for the vessel. It is sea state and depth independent and defined in nine directions from 0 to 180° considering symmetry about the x-y plane. The plot 5.4 shows pitch and heave motion. Their phase is almost 90 degree and 0 degree respectively – figure 5.5. It must be noted that this is an example RAO for RIFLEX, and thus no documentation around the vessel or turret is given. RIFLEX uses the motion data in its global coordinate system with a vertical offset of $Z_g = -1.97m$.

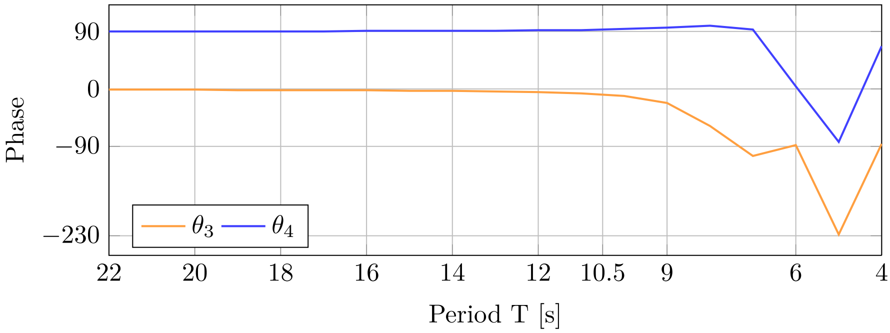

Figure 5.5: The phase for the RAO - head sea (180°)

5.2.3 Environmental conditions

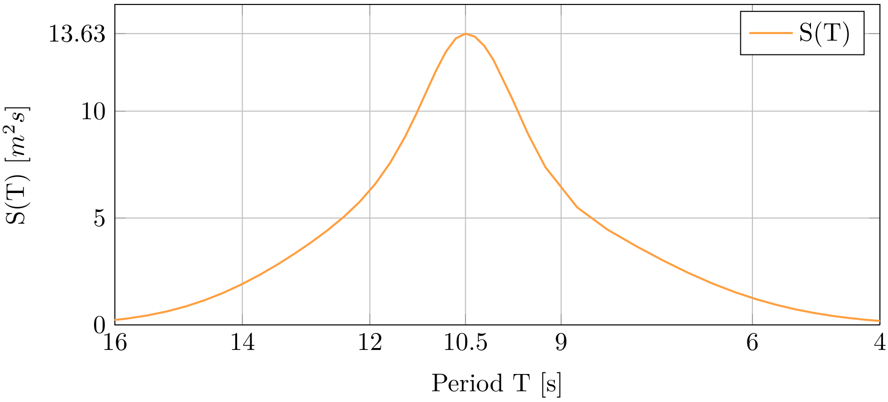

Figure 5.6: The spectral density function JONSWAP – plotted for load case 8 $H_s = 3.0m$ $T_p = 10.5s$

The weather data applied in this project comes from a technical specification for the Campos Basin (2005). The distribution of total *significant wave heights* (H_{s1}) and primary spectral periods (T_{p1}) is applied. The source of the scatter diagram is Campos Basin data (PROCAP1, PROCAP2., P-18 and P-25) . The wave data was tabulated at 3-hour intervals, providing information equivalent to 40824 hours (= $13608 \cdot 3$ hours). The scatter diagram is given in table 5.4 with the color codes defining the load cases.

Since the scope of the project is to do a qualitative comparison between three different models; current, wave and offset are left out to reduce the number of load cases. Furthermore, no spreading function is used. The theory is still presented here to give an orientation on the subjects usually addressed.

Wave spectral density function

The specification presents a *modified* JONSWAP spectrum to use with the scatter diagram. The modification is most noticeable in the fact that γ, the parameter of the function's peakedness, is only dependent on T_p.

- H_s – the significant wave height.
- T_p – the spectral peak period.
- T_z – the zero-up-crossing period.

$$S(\omega) = \frac{5}{16} \cdot H_s^2 T_p \left(\frac{\omega_p}{\omega}\right)^5 (1 - 0.287 \ln \gamma) \exp\left(-1.25 \left(\frac{\omega}{\omega_p}\right)^{-4}\right) \gamma^{\exp\left(-\frac{(\omega-\omega_p)^2}{2(\sigma\omega_p)^2}\right)} \tag{5.1}$$

$$\gamma = 6.4 \cdot T_p^{(-0.491)} \tag{5.2}$$

$$T_z = T_p \sqrt{\frac{5+\gamma}{10.89+\gamma}} \tag{5.3}$$

$$\sigma = \begin{cases} 0.07 & \omega \leq \omega_p \\ 0.09 & \omega > \omega_p \end{cases} \tag{5.4}$$

Wave spreading

Directional wave spreading is important to assess, as short-crested waves could often lead to more fatigue than long-crested. The basic assumption is that the directional spectral density function is the product of an *angular spreading function*, $D(\beta)$ and the one-dimensional Jonswap (eq. 5.5). DNV [2011] proposes the wave spreading function $D(\beta) = \cos^2(\beta)$ to be used for both fatigue and ultimate strength analysis.

$$S(\omega, \beta) = S(\omega) \cdot D(\beta) \tag{5.5}$$

Current

The current profile through the depth of the ocean can be readily obtained from the weather report. In a complete analysis it should be evaluated, however it is proposed that for shallow water this will be a minimal contribution to fatigue and not make a qualitative difference for the results. It should be noted that if current was included in an angle different from head-sea, one would need to look at hang-off angles in both the x and y planes and that the BFLEX angle models would need to bend in both planes. The methodology for the models is further explained in 6.2.

Vessel mean offset

The vessel can drift off position by waves, current and wind. In addition vessel positioning error can be a factor. Offset is accounted for in analysis as typical *worst cases*, and they are assessed as a static offsets for a whole analysis. The upper offset for an intact mooring system on 125 meter water depth can be in the range of 20 meters (Sævik).

The system's design shape is either stretched, which is dubbed *far* or compressed which is dubbed *near*. In the same manner it could be relevant to account for *transverse* drift as well. In particular in extreme wave analysis this is important to assess. In figure 5.8 one can see a scenario where the vessel is off position in a unfavorable way that exerts high mean tension and high mean moments on the termination end at hang-off as well as on the seabed. Even emergency shutdown and disconnection could be necessary in such scenarios.

A *far* offset can induce a mean tension that reduces the curvature response. The fatigue damage in tensile armor is found to be more affiliated to curvature than tension (ref. chapter 8). An offset could thereby reduce the fatigue response. It is comprehensible that the opposite can happen for a *near* offset. In any way, it is important to be aware of the *mean stress effect* presented in section 4.6.4, thus the definite answer to what contributes most to fatigue is not readily clear for every case.

Applying symmetry, it is therefore practice that every heading needs to be repeated six times i.e no offset, *near* and *far* with or without *transverse* drift. In conclusion the number of relevant sea state and vessel position scenarios for a commercial project can be extensive.

5.2.4 Blocking of the scatter diagram.

The wave scatter diagram needs to be blocked, or grouped together, because running every single sea state as is would not just require a lot of time, but it could be unnecessary because the contribution to fatigue damage is not evenly distributed. The intention of the blocking is therefore to sort the sea states into a given number of representative wave classes so that one can get a similar result that is fitting and not too conservative.

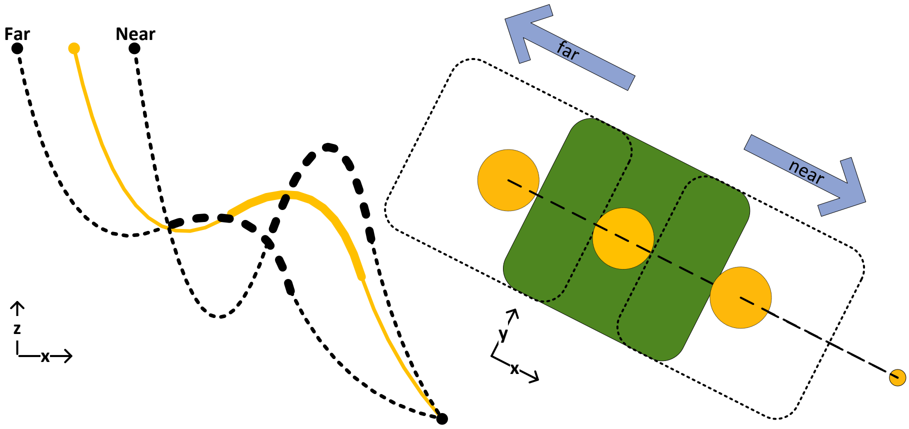

Figure 5.7: The offset away from the TDP is dubbed *far* while towards is *near* (not to scale)

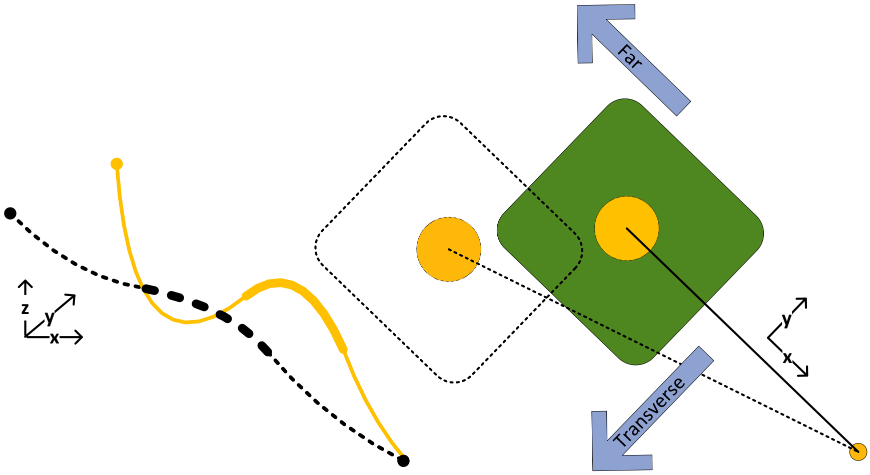

Figure 5.8: An extreme scenario where the vessel is off position both far and transverse.

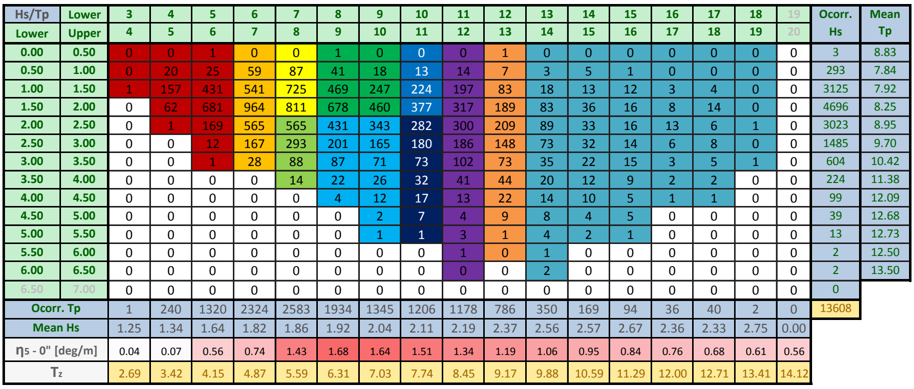

Hs/Tp	Lower	3	4	5	6	7	8	9	10	11	12	13	14	15	16	17	18	19	Ocorr. Hs	Mean Tp
Lower	Upper	4	5	6	7	8	9	10	11	12	13	14	15	16	17	18	19	20		
0.00	0.50	0	0	1	0	0	1	0	0	0	1	0	0	0	0	0	0	0	3	8.83
0.50	1.00	0	20	25	59	87	41	18	13	14	7	3	5	1	0	0	0	0	293	7.84
1.00	1.50	1	157	431	541	725	469	247	224	197	83	18	13	12	3	4	0	0	3125	7.92
1.50	2.00	0	62	681	964	811	678	460	377	317	189	83	36	16	8	14	0	0	4696	8.25
2.00	2.50	0	1	169	565	565	431	343	282	300	209	89	33	16	13	6	1	0	3023	8.95
2.50	3.00	0	0	12	167	293	201	165	180	186	148	73	32	14	6	8	0	0	1485	9.70
3.00	3.50	0	0	1	28	88	87	71	73	102	73	35	22	15	3	5	1	0	604	10.42
3.50	4.00	0	0	0	0	14	22	26	32	41	44	20	12	9	2	2	0	0	224	11.38
4.00	4.50	0	0	0	0	0	4	12	17	13	22	14	10	5	1	1	0	0	99	12.09
4.50	5.00	0	0	0	0	0	0	2	7	4	9	8	4	5	0	0	0	0	39	12.68
5.00	5.50	0	0	0	0	0	0	1	1	3	1	4	2	1	0	0	0	0	13	12.73
5.50	6.00	0	0	0	0	0	0	0	0	1	0	1	0	0	0	0	0	0	2	12.50
6.00	6.50	0	0	0	0	0	0	0	0	0	0	2	0	0	0	0	0	0	2	13.50
6.50	7.00	0	0	0	0	0	0	0	0	0	0	0	0	0	0	0	0	0	0	
Ocorr. Tp		1	240	1320	2324	2583	1934	1345	1206	1178	786	350	169	94	36	40	2	0	13608	
Mean Hs		1.25	1.34	1.64	1.82	1.86	1.92	2.04	2.11	2.19	2.37	2.56	2.57	2.67	2.36	2.33	2.75	0.00		
η_5 - 0" [deg/m]		0.04	0.07	0.56	0.74	1.43	1.68	1.64	1.51	1.34	1.19	1.06	0.95	0.84	0.76	0.68	0.61	0.56		
T_z		2.69	3.42	4.15	4.87	5.59	6.31	7.03	7.74	8.45	9.17	9.88	10.59	11.29	12.00	12.71	13.41	14.12		

Table 5.4: Distribution of Total Significant Wave Heights and Primary Spectral Peak Periods. Color codes are the load cases applied.

The stress in the tensile armor is assumed proportional to the curvature, which again is assumed to be proportional to the angle deflection between the riser and the point of suspension – *the hang-off angle.* As such dynamic analysis can be used to determine which peak periods (T_p) that give the largest hang-off angles.

For most cases, it will be a good correlation between the response of the ship and the hang-off angle. For the purpose of this study. It was assumed that the ship's RAO gave a sufficient picture of the critical responses which would require finer blocking. The Palmgren-Miner linear damage rule is employed, and the following relation seen in equation 5.6 is obtained.

$$D = \frac{n_i}{N_i} = \frac{n_i}{a\Delta\sigma_i^{-m}} = n_i a \Delta\sigma_i^m \propto n_i a \Delta H_i^m \tag{5.6}$$

Where H is the transfer function. With this assumption, one can define an impact value. This is proposed to be the probabilty density function (PDF) of one column multiplied with the vessel's RAO to m.

$$I = P[a \leq T_p \leq b] \cdot \Delta H_5^m \tag{5.7}$$

- Where the values are small, as they are on the extremities of the diagram: The periods can be lumped together in bigger blocks.
- Where the values are high: It is important to separate vertically, as they will likely dominate the fatigue damage.

The blocking is done for head-sea only, since this analysis will only encompass head-sea. In general every heading needs different blocking, since coupled motions can give quite diverse motion characteristics for the same sea. The scatter diagram ended up being divided into eleven wave classes.

- Group one and eleven are lumped because of low probability and low impact value.
- Group five and six comprise two peak periods because the response difference between $T = 8.5$ and $T = 9.5$ is marginal.
- The wave classes from period six to ten seconds are divided and vertically divided into two blocks as they are anticipated to dominate the fatigue result based on their high probability and high response (high impact value).

To obtain a *representative significant wave height* of each block, the safest way would be to use the highest one. The drawback of this is that it will lead to very conservative results. In this study, the weighted mean of the wave heights to the power of m is taken as the representative wave. It is not necessarily true that the wave height is proportional to the fatigue damage (stress). In particular with irregular sea and shallow water the system exercises a lot of non-linear dynamics. It is proposed that if the wave classes are sufficiently refined this will not be erroneous, yet it is important to be aware of this. To capture the non-linearity, dynamic analysis could be done to obtain the hang-off angle for increasing wave heights and weight the mean on this.

The *representative wave periods* for the two lumped blocks east and west in the diagram were found by weighted average to the respective occurrences of each period comprised in the block.

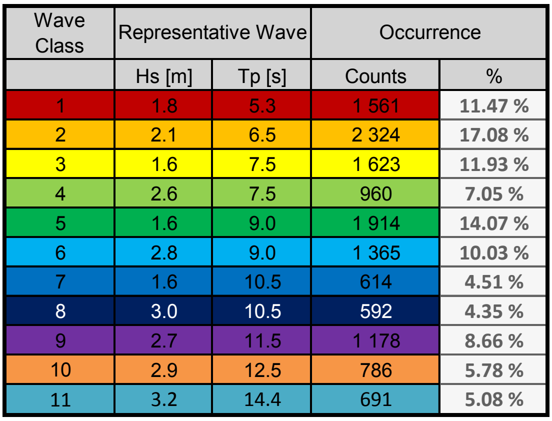

Wave Class	Representative Wave		Occurrence	
	Hs [m]	Tp [s]	Counts	%
1	1.8	5.3	1 561	11.47 %
2	2.1	6.5	2 324	17.08 %
3	1.6	7.5	1 623	11.93 %
4	2.6	7.5	960	7.05 %
5	1.6	9.0	1 914	14.07 %
6	2.8	9.0	1 365	10.03 %
7	1.6	10.5	614	4.51 %
8	3.0	10.5	592	4.35 %
9	2.7	11.5	1 178	8.66 %
10	2.9	12.5	786	5.78 %
11	3.2	14.4	691	5.08 %

Table 5.5: Load case definitions for the global model. The color codes are coherent with those in the scatter diagram in table 5.4

5.3 Global riser model in RIFLEX

The riser and buoyancy modules were the first things to get modeled in RIFLEX. The bending stiffener was appended afterwards after seeing what kind of dynamic motions the system will be submitted to. The riser was modeled as a 250 meter line clamped to the seafloor, it was desired that a part of the pipe would be lying free on the seafloor to avoid any forced motion onto the system from the restraint. Aside from the riser, two dummy elements were modeled out from the vessel to be able to capture the hang-off angle variations. Figure 2.5 illustrates the shape of the system.

Nondimensional hydrodynamic coefficients were used in RIFLEX. A fully submerged cylinder with no end-effects was considered i.e added mass and drag in the normal direction. In RIFLEX the force coefficients are defined as in equations 5.9 and 5.8 for added mass and drag respectively. C_{mn} and C_{dn} were set equal to one. No other effects were considered.

$$C_{Dy} = \rho \frac{D}{2} C_{dn} \tag{5.8}$$

$$A_{My} = \rho \frac{\pi D^2}{4} C_{mn} \tag{5.9}$$

5.3.1 Buoyancy modules

A design report of a buoyancy module was not available to the author. The specific physics of the modules are not relevant in the project, so this step is to model something simple without running into trouble with convergence in the software. As such, the buoyancy modules were modeled as an independent continuous segment in RIFLEX. It was given its own geometry and density whereas EI, GT and EA were set to the same values as the riser's. The material density was set to $600\frac{kg}{m^3}$, and the length of the whole segment was set to 50 meters. The outer diameter was calculated in excel to get suitable buoyancy. The system was then solved statically in RIFLEX to verify the form and clearance to seabed. The outer diameter was corrected a bit, and in the end set to 1 meter. A run with a head-on harmonic wave of $H = 5[m]$ and $T = 10[m]$ was conducted

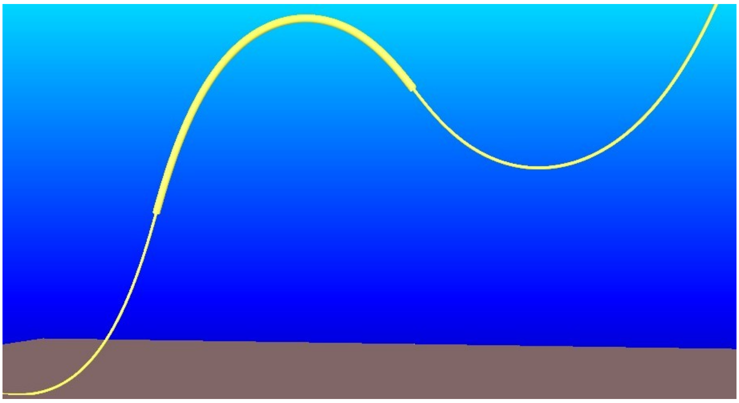

Figure 5.9: The buoyancy modules

to check the motion and functionality of the configuration.

5.3.2 Bending stiffener

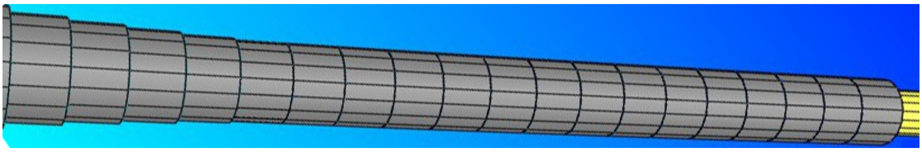

Figure 5.10: Bending stiffener in GLview

The bending stiffener is made of molded polyurethane elastomer, which span a wide range of mechanical properties and is highly dependent on temperature. Again a design report was not available. $E = 150$ MPa was obtained from an earlier KOGT project for Statoil on Troll B, and the material is assumed linear. The density was set to $1200\frac{kg}{m^3}$. Running the dynamic analysis, it was found that the highest effective tension from the load cases was around 210kN, and retrospectively the taper was sized to take a tension of 250kN ($\approx +20\%$) at an angle of departure of 8 degrees.

The stiffener has been modeled in RIFLEX by discretization, it is divided into 20 segments of one element each. The length of each piece is then 0.35[m]. The TAPER tool, which is a static FE script for Excel developed by KOGT, was used to find the right contour over the elements. A 7 meter stiffener was proposed. The external diameter top was set to OD + 65 mm which is justified by a stiffener tip of 35 mm and a wall clearance of 15 mm to each side of the riser, which were numbers taken from the already mentioned project on Troll B.

By now all necessary input to TAPER was known except for the root diameter. In calculating the stiffener, it is relevant to also include the EI from the internal pipe. The following plots show bending stiffener characteristics; moment and curvature from the TAPER tool. Moreover the figure 5.10 shows the stiffener in GLview. It can be noted that the BS will appear more stiff in a static model. The load cases were conducted with this dimension.

The responses oscillate almost around zero curvature, a bit skewed towards the negative curvature. This is because the sagbend goes to positive curvature and thus demands more response in the opposite direction on the bending stiffener. However, this is a small difference and therefore the *ranges* of the curvature envelopes are ideal to represent the different sea states in a simple plot. This can be seen in figure 5.12. It seems like it is performing good. The root thickness was held at one meter.

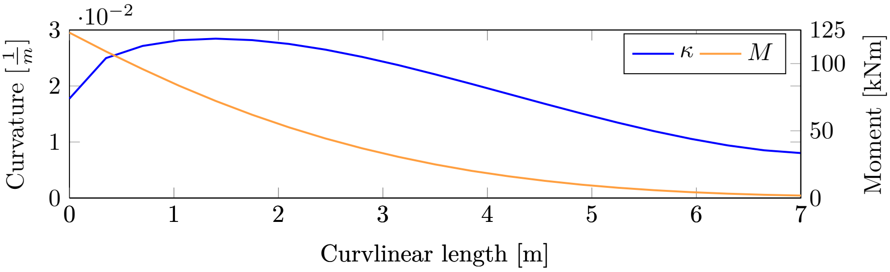

Figure 5.11: Static: Moment and Curvature over length – 8° departure angle and a pull of 250kn. 20 elements.

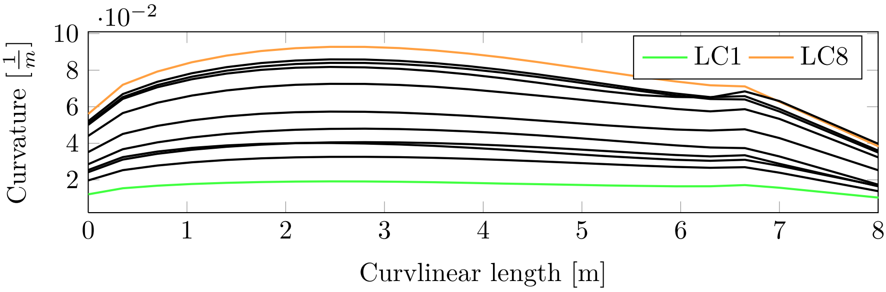

Figure 5.12: Dynamic: The range of bending stiffener envelopes for the 11 different sea states. LC8 is the biggest, LC1 the smallest.

5.4 M1 – The stub model in BFLEX

The stub model is a two element model which uses the moment formulation to represent a cutout of the riser. It is submitted to the curvatures and tension which were found at the most extreme part the bending stiffener, noting that the bending stiffener is *not* modeled here. It is important that the distance e in 5.13 is small. This is because this distance spurs secondary bending moment.

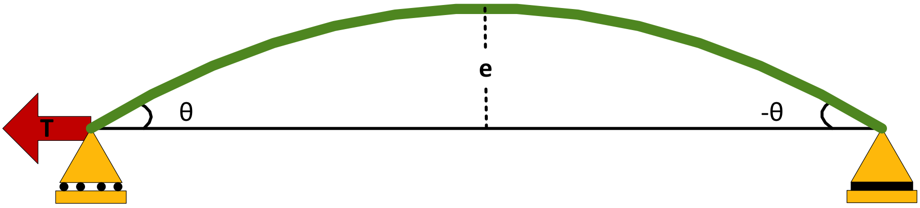

Figure 5.13: **M1** – The stub model is modeled as a simply supported beam

For a simply supported beam the relation between curvature and nodal rotation is given as in equation 5.10. With this, the element curvature from RIFLEX can be transformed to prescribed rotations in the left and right corner of the model. The length overall was set to $200[mm]$ thus the curvature was used with a factor of $\frac{0.2}{2}\kappa = \theta = \frac{\kappa}{10}$. The tension is added as a leftbound nodal load on the roller support.

$$\kappa = \frac{2\theta}{l} \tag{5.10}$$

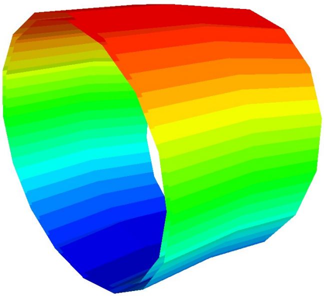

Figure 5.14: **M1** – The stub model in Xpost showing the two tensile armor layers – colors show curvature.

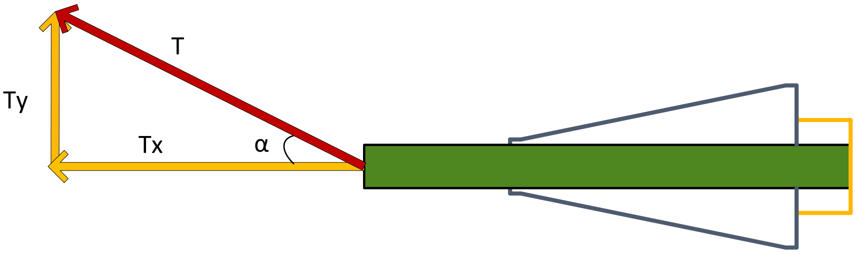

Figure 5.15: **M2 & M3** – Principal sketch of pipe with BS and guidetube with force vectors. α is the hang-off angle subtracted the static offset (eq. 5.11).

5.5 M2 & M3 – The hang-off angle models in BFLEX

Both the second and third model use the same principal, but with different ways of modeling the elements. It is assumed that the pipe has zero curvature in the hanging part between the top section and the sagbend – it is straight owing to the tension in the system. It is proposed that it can be used as a reference point to measure the angle between the point of departure on the vessel and the pipe. See the figure on page 73 for an illustration. The hang-off angle and tension is taken from such an element, for instance 30 meters down pipe. The angle α is the angle between the element subtracted the static hang-off angle off the x-axis, $\beta_0 = 82°$ (eq. 5.11).

$$\alpha(t) = \beta(t) - \beta_0 \tag{5.11}$$

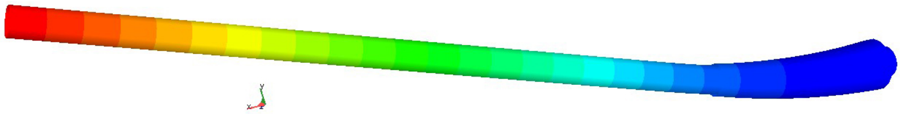

Figure 5.16: The hang-off angle model in Xpost, colors show y-displacement

The tension is decomposed to an axial and a lateral force and are put on as nodal forces on the bending stiffener model. In static equilibrium (fig. 2.5) the riser's top section and its intermediate part will be a straight section making the hang-off angle equal the riser's angle of departure – close to 82 degrees. The time series for the hang-off angle is therefore subtracted these 82 degrees to only have the varying angle ($\alpha = 0$ at $t = 0$). As such, the models in BFLEX can be interpreted as horizontal beams as illustrated in figure 5.15.

There were some end-effects in the ITCODE0 model whose cause was proposed to come from the lack of zero curvature by the restraint. As such M2 and M3 were remodeled with a guidetube 0.5 meters out from the the restraint to better assess this effect. The guidetube's bending stiffness was scaled to match that of the end of the bending stiffener, to provide a smooth change-over. As such, the BS differs from the one in the global model.

(a) without guidetube (b) with guidetube

Figure 5.17: The difference in damage by wall restraint ITCODE0-model

5.5.1 M2 – ITCODE31

The ITCODE31 model is modeled in one stretch from 0 to 30 meters as illustrated in figure 5.18.

Figure 5.18: **M2** – A conceptual sketch of the BS model with ITCODE31

5.5.2 M3 – ITCODE0

The sandwich formulation is more demanding numerically, therefore the model is split into a 10 meters piece with ITCODE0 elements and 20 meters of standard pipe elements with the bending stiffness equal the pipe in stick. Stick stiffness is used because this part of the riser should has close to zero curvature.

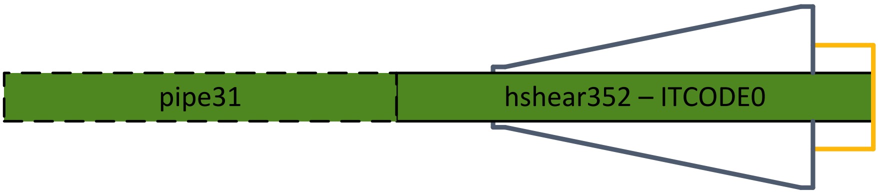

Figure 5.19: **M3** – A conceptual sketch of the BS model with ITCODE0

5.5.3 M3X – Independent nodal systems

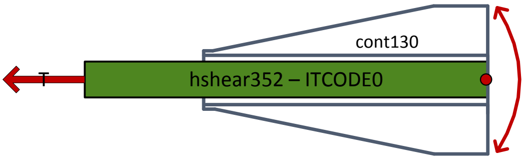

Figure 5.20: **M3X** – Independent nodal systems for the BS and the pipe. Prescribed rotations is applied on both the BS and the pipe at the root while the pipe is tensioned with a axial force at the tip. It should be noted that this load pattern is not the same as the other models.

The M3X was decided after the results from the M3 model was obtained. In M3, the transition from zero curvature to curvature gives an intense fatigue response for the tendons. It was proposed that this response was because the nodal displacement is governed by the BS and not the pipe. This leads to the very abrupt motion of the tendons when the BS, element by element, reduces its bending stiffness and increases its susceptibility to bending. It was thought that this could be solved by modeling the pipe and the BS into *two independent nodal systems*. As such the tendons would have the ability to have a more distributed displacement. It is thought that the damage obtained in the hotspot would then be spread over a larger area. The full model which was set up to assess this, *M3X*, was not successful. The author could not get the contact elements to give proper convergence. The original M3X is presented in appendix A. Instead, a more simplified loading was conducted on the same model. Prescribed rotations around the root and a tension force at the pipe-tip. This model converged.

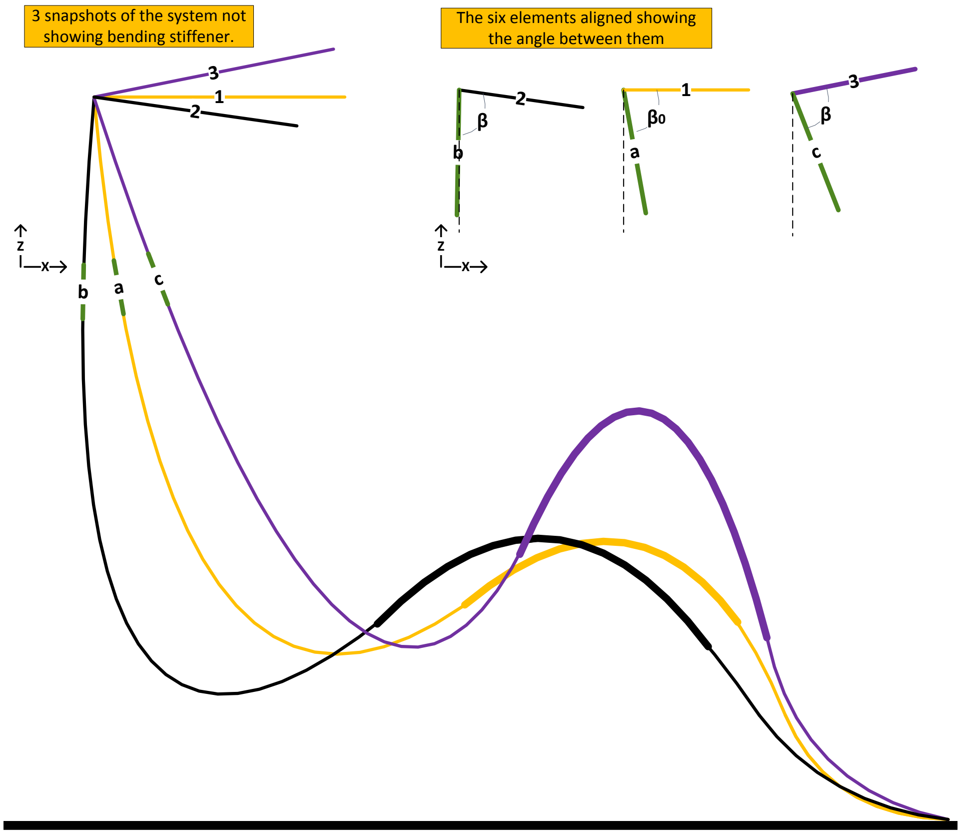

The element in position a,b and c are assumed to have zero curvature thus serve as a reference point. The dot product between this and a dummy element in position 1,2 and 3 will then give the hang-off angle. Position (a,1) is $t = 0$ with $\beta_0 = 82°$. Heave motion is not shown.

5.6 On- and offloading in BFLEX

The loads and prescribed rotations are ramped as a smooth half-cosine, which BFLEX recommends for wave loads (Sævik [2013]). The models are submitted to internal pressure and axial load before the *TIMEINI*-event. This is the load step where the stick-slip properties of the friction springs between the layers in the cross-section are calculated. This TIMEINI needs to be on a load step after the pressure and axial loads are finished, but before bending loads (i.e lateral loads).

The load procedure is done in the models as illustrated in figure 5.21. The internal pressure is applied in full before the mean tension is ramped on. After this the mean tension is ramped on up to the orange line, which is the TIMEINI-event. The lateral load T_y is then ramped on, while the same tension is kept. When T_y has reached its mean, both loads follow the same sequence of on- and offloading. For the stub model, the tension and prescribed rotation are applied with the same principle.

The maximum and minimum are set as half of the range around the given mean tension or curvature. Because of non-linear effects the load sequence is repeated several times. It is important that the model *settles*. The effect can be confirmed by plotting the cyclic stress and curvature through the time steps. The purple line defines the start of the actual fatigue calculations.

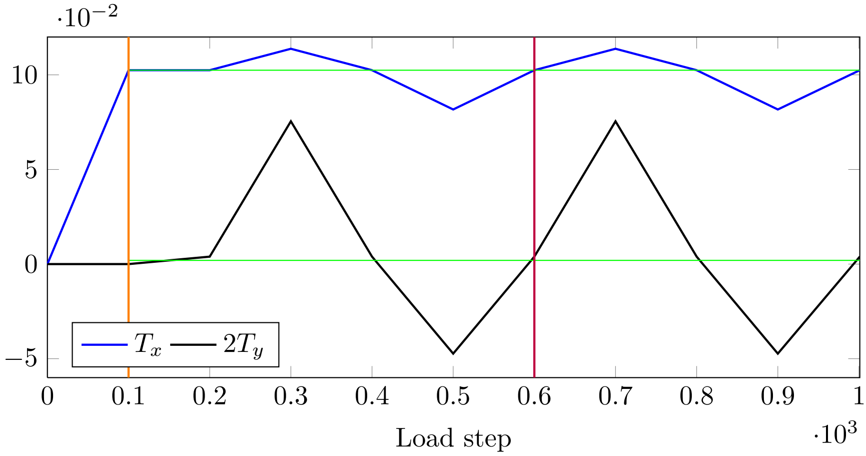

Figure 5.21: The load model applied. Orange line indicates TIMEINI and the purple line indicates the start of fatigue calculations.

6 | Results

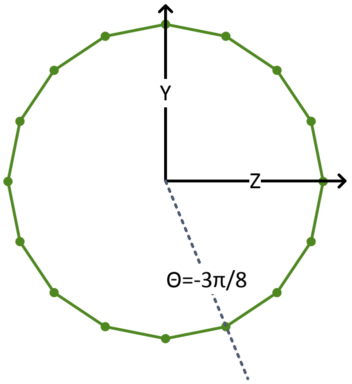

Figure 6.1: Intergration point naming convention used herein. Local node 1 is the bottom node ($\theta = -\frac{\pi}{2}$), while the top node is number 9 ($\theta = \frac{\pi}{2}$). The counting is clockwise. The results are from the inner tensile armor if nothing is specified, thus $r = |133.8|[mm]$

6.1 M1 – The stub model in BFLEX

- Highest yearly fatigue is found at $(x, \theta) = \left[0, \frac{\pi}{2}\right]$ with $D = 0.01277[y^{-1}]$. The number of years to instant break is then $0.01277^{-1} = 78$.

It gets the most damage on the tension side as it oscillates about an average curvature. Ideally both the full restraint and the roller side would have an equal damage; the damage is less and not equal on the roller side because of the secondary bending moment which is induced from the tension. Reducing the length will reduce the curvature with the same relation (eq. 5.10). Therefore, this effect can not be eliminated in this type of model.

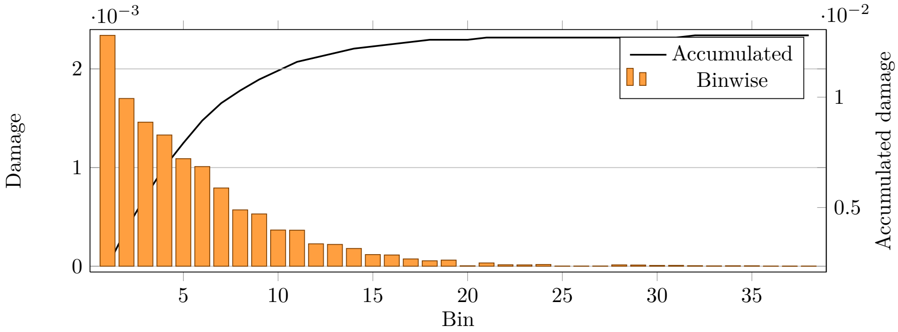

Figure 6.2: **M1** – The fatigue contribution from the different bins at $(x, \theta) = \left[0, \frac{\pi}{2}\right]$

6.1.1 Measure the fatigue before stabilization

From a modeling point of view one is inclined to speed up the solution time, thus cutting number of cycles. It was therefore interesting to see what would happen if one measure the fatigue before the model has settled. As can be seen in figure 6.4 the response stabilizes after the third cycle.

It is found that calculating fatigue through the unsettled third cycle (181 to 281) leads to a nonconservative result. It gives the same trend of fatigue distribution, however the total damage accumulates to $D = 0.010803[y^{-1}]$ and the fatigue contribution from the blocks is completely different. The result is an overestimation of the fatigue life by 18%.

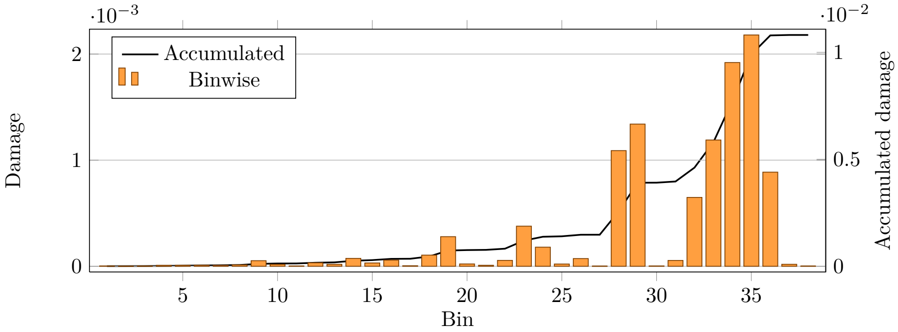

Figure 6.3: $\tilde{\mathbf{M}}\mathbf{1}$ – Unsettled run, the fatigue contribution in node 9.

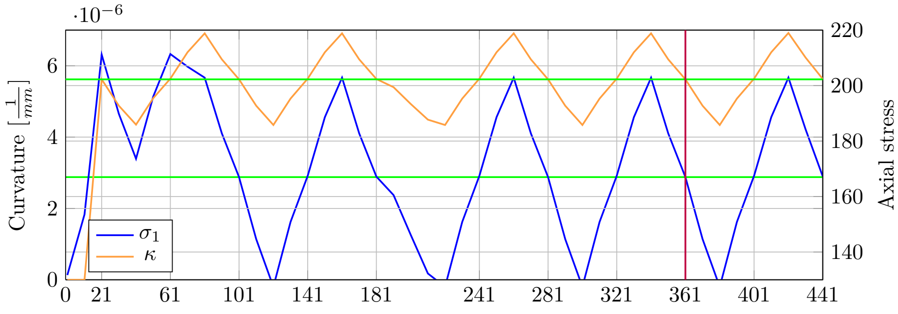

Figure 6.4: **M1** – Model settles on fourth cycle. The purple vertical line indicates the fifth cycle, where fatigue calculation starts.

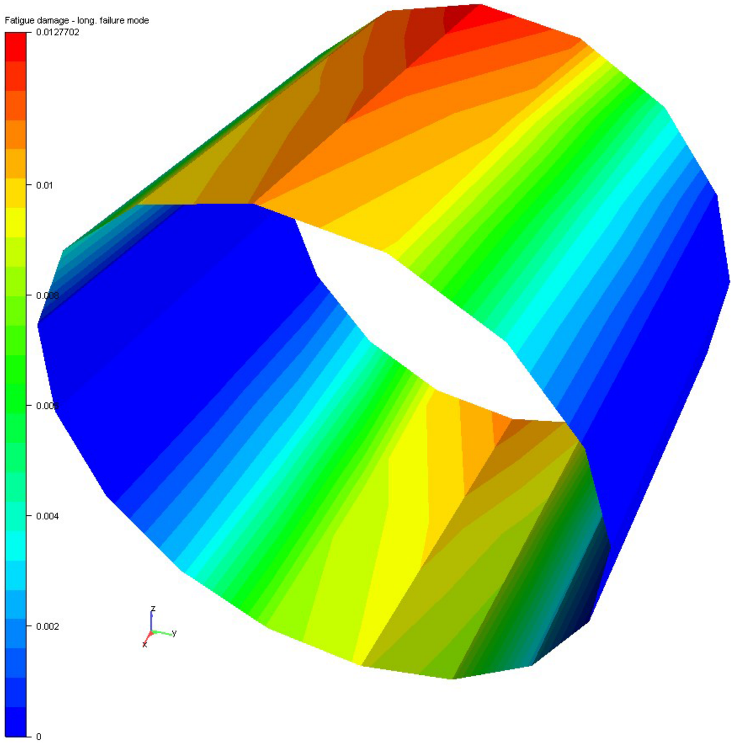

Figure 6.5: Accumulated fatigue distribution for the inner tensile armor. Color scale $\in [0, 0.01277]$

6.2 M2 & M3 – The angle models in BFLEX

Most damage is found in the top and bottom of the pipe cross-section, as expected. The damage in the bottom is bigger because of the average loading that makes the pipe have a constant bend to this side. It was anticipated that maximum damage would be at $x \approx 3[m]$ since this was were the maximum curvature was found in the RIFLEX model. The peak is however skewed towards the tip, which indicates that the bending stiffener is too stiff in the BFLEX models. Figures 6.8 and 6.11 further confirm that both models suffer an abrupt change-over. This is either an indication of too much bending loads in comparison to the tension or too stiff BS. The latter is the most reasonable.

6.2.1 M2 – ITCODE31

- Disregarding the BS-tip peak – M2 has the lowest absolute fatigue. Negligible fatigue in outer armor.
- Highest yearly fatigue in the domain $x < 7.0[m]$ is found at $x = 4.61[m]$ with $D = 0.00653[y^{-1}]$. The number of years to instant break is then 153.
- Absolute highest damage (at BS-tip) is $\tilde{D} = 0.00747$.
- The peak fatigue in bottom is symmetrically located on each side of the lowest point, $\theta = -\frac{3\pi}{8} \cup -\frac{5\pi}{8}$
- At BS-tip: high difference in curvature i.e plastic behavior over a short length is included in fatigue calculations which results in spike there.

6.2.2 M3 – ITCODE0

- Disregarding hotspot – Highest yearly fatigue in the domain $x \geq 0.75[m]$ is found at $x = 4.10[m]$ with $D = 0.00803[y^{-1}]$. The number of years to instant break is then 124.

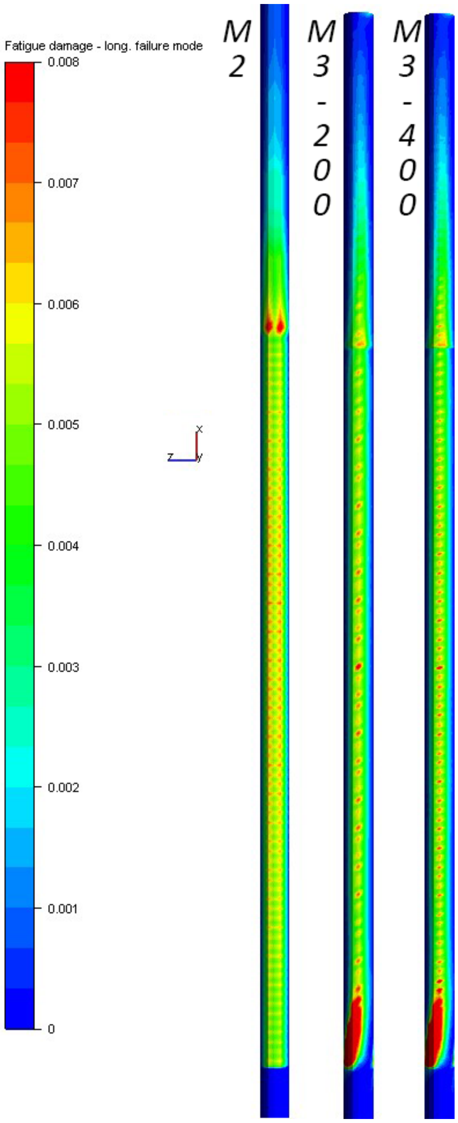

M2 & M3 200/400 elements – Accumulated fatigue distribution on the compression side. Positive y is out of plane. Color scale $\in [0, 0.008]$

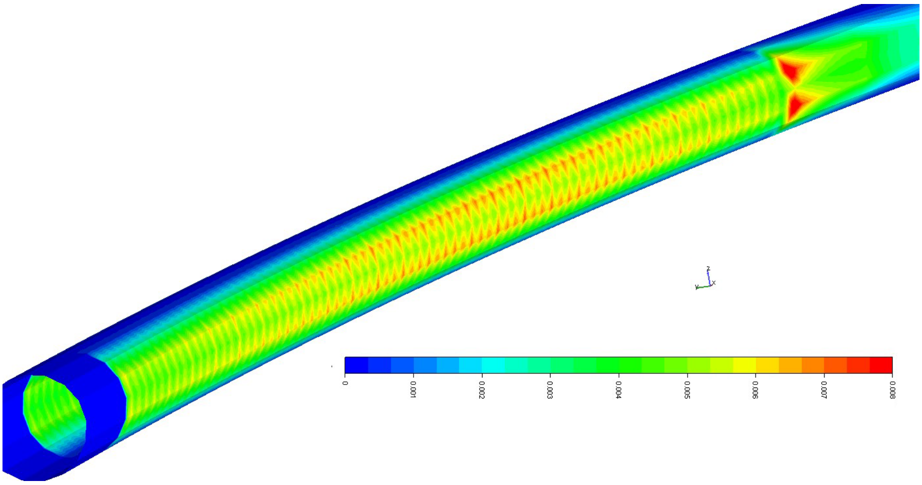

Figure 6.6: **M2** – Accumulated fatigue distribution. On the compression side. The figure demonstrates the symmetry about the bottom integration point and the peak damage at the tip. Color scale $\in [0, 0.008]$

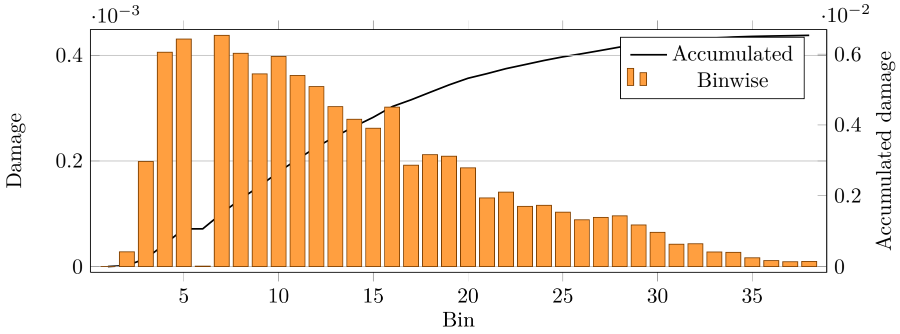

Figure 6.7: **M2** – The fatigue contribution from the different bins at $(x, \theta) = \left[4.61, -\frac{3\pi}{8}\right]$

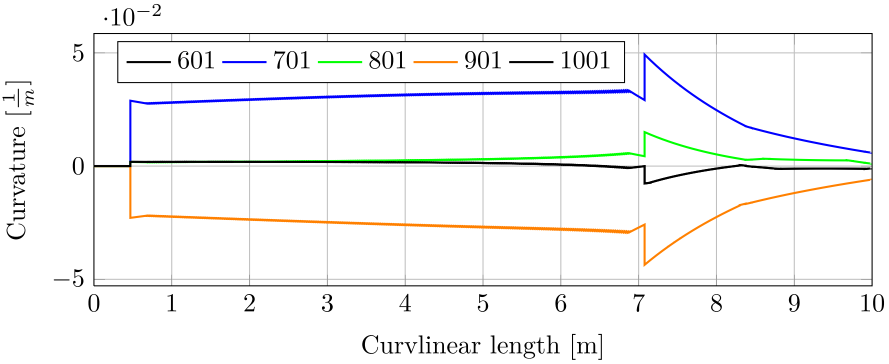

Figure 6.8: **M2** - Curvature response for bin 38 for one cycle. The figure shows abrupt change in the transition at BS-tip.

- Absolute highest damage (in hotspot) is $\tilde{D} = 0.0264$.
- The peak fatigue in bottom is located in the lowest integration point.
- It can be seen from figure 6.11 that the model has significant motion at the guidetube.
- The transition from restrained to curved pipe spurs concentrated movement of the tendons in this zone which leads to very high fatigue. This damage is seen again in the outer tensile armor 90° of the bending direction.
- At BS-tip: the tendons pass the tip without the spike in fatigue as seen in M2 as their movement is more unrestrained to the high curvature response here.

M3 – mesh refinement

The choice of $50[cm]$ elements (200 elements over 10 meters) to M2's $23.3[cm]$ (300 elements over 7 meters) was decided primarily because it was thought that

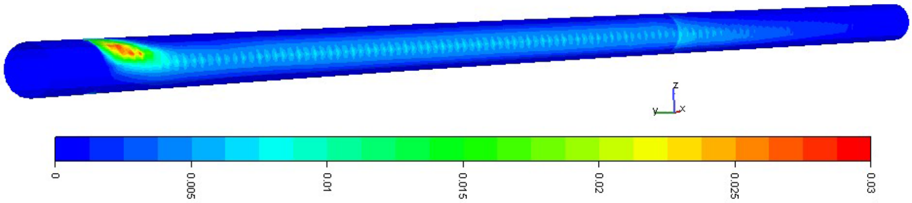

Figure 6.9: **M3 200** inner tensile layer – Hotspot at the transition goes along the bending action. Color scale $\in [0, 0.03]$

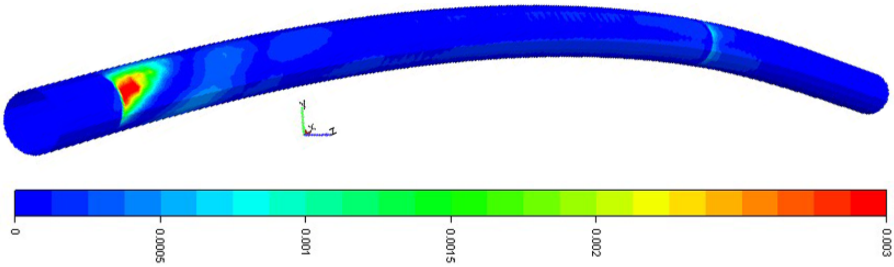

Figure 6.10: **M3 200** outer tensile layer – In the second layer the hotspot damage is 90° on the inner layer. Color scale $\in [0, 0.003]$. Note, ten times smaller scale.

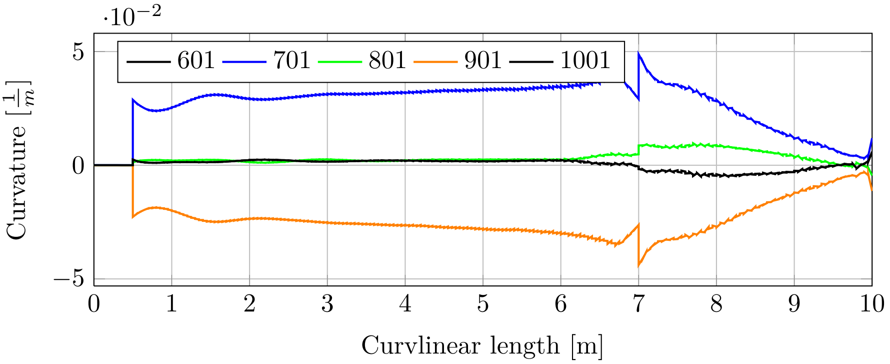

Figure 6.11: **M3 200** – Curvature response for bin 38 for one cycle. The figure shows abrupt change in the transition at BS-tip and motion by the guidetube.

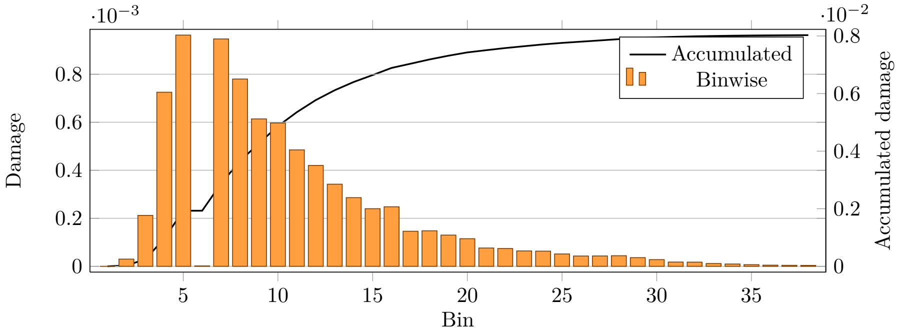

Figure 6.12: **M3 200** – The fatigue contribution from the different bins for $(x, \theta) = \left[4.10, -\frac{\pi}{2}\right]$

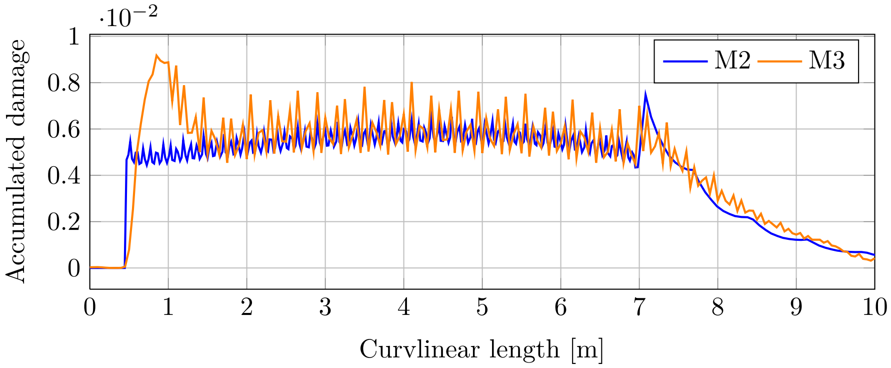

Figure 6.13: **M2 & M3 200** – Accumulated damage in bottom of pipe over the length for points on the pipe's underside, $\theta_{M2} = -\frac{3\pi}{8}$ and $\theta_{M3} = -\frac{\pi}{2}$

the tendon model could produce the same results with less resolution seeing that it has a more true-to-nature model. However the plot of the damage along the length seemed very jagged in comparison to M2. It was decided to do a run with $25[cm]$ elements as well.

- Highest yearly fatigue in the domain $x \geq 1.1[m]$ is found at the same point: $x = 4.10[m]$ with $D = 0.00801[y^{-1}]$. A reduction of 0.25%
- Absolute highest damage (in hotspot) is $\tilde{D} = 0.02792$. An increase of 5.5%.
- The damage of the hotspot is even more distributed around the cross-section without decreasing the peak damage.

M3X – Independent nodal systems

The fatigue damage in M3X also shows the pronounced hotspot damage (fig. 6.15b). Since the load condition was different, the same loading was applied on M3 to confirm that rotation about the root also creates the hotspot in M3. This

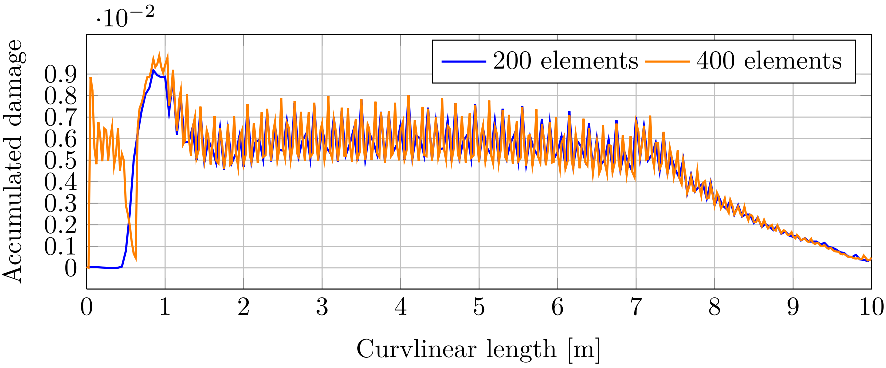

Figure 6.14: **M3** – Comparison of accumulated damage between 200 and 400 elements.

was proved to be true, seen in figure 6.15b.

(a) **M3X** – hotspot damage at the root (b) **M̃3** – still shows the same tendency.

Figure 6.15: Hotspot assessment – Inner tensile armor on the pipe to the left, while outer tensile armor on the right. The color scales for each pipe are not coherent. The damage on the inner layers is several times higher.

7 Discussion

7.1 Blocking of the scatter diagram

The blocking of the scatter diagram is not optimal. The intention is that the blocking is done in such a way that each bin gives similar damage. This is not the case, the trend for all cases is that the damage is bigger for the highest cycles. The tension is almost constant through all the load bins, which is understandable because the chief contributor to the tension is the system's static weight.

The bins 1,2,3,4 and 6 which oppose this trend for M2 and M3 have all in common that they have very low tension and thereby low lateral load, which explains that the damage from these bins do not add up much. The results are decreasing with increasing bin number, which are sorted on cycles from high to low. This is almost the same as sorting the hang-off angle from low to high (in reference to the range spectrum in figure 4.7). Bin 38 has a lateral force that is ten times bigger to that of bin 4, however bin 4 is cycled 1200 times more.

M1 shows the same trend but is even more pronounced. Almost all the damage for M1 is found in the initial bins for the same reasons as M2 and M3. Bin 38 has a curvature a little over four times to that of bin 1, whereas bin 1 is cycled 3000 times more.

The peak period weighted to the power of m is the method used herein. However, a foul in this approach could be that the actual fatigue response could be more dependent of T_z, the zero-up-crossing period. Maximum pitch motion for the vessel is $T = 9[s]$. A given sea state of $T_p = 12[s]$ has $T_z = 8.8[s]$ thus could contribute to more fatigue than a sea state with $T_p = 9[s]$.

More time should have been spent analyzing the response in the global model. The assumption that the actual hang-off angle is closely related to that of the vessel's RAO in pitch should be revised. This can be a source of error.

7.2 M3 & M3X – Assessment of hotspot

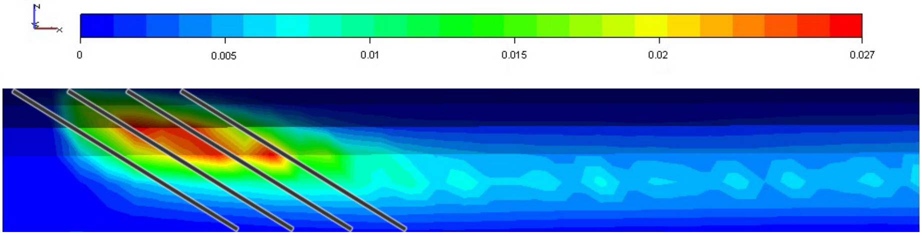

Figure 7.1: **M3** – The hotspot with tendons illustrated as straight lines with $\alpha = 31.6°$. Color scale $\in [0, 0.027]$

M3X, shown in figure 6.15a, demonstrates that the hotspot effect goes back to the wall restraint, which was the issue before applying the guidetube. This is coherent with the idea that the contact between the bending stiffener and the pipe is gone. Figure 6.15b confirms that this type of prescribed rotation still gives the hotspot at the transition between the guidetube and the BS.

All the suggested ways of modeling the ITCODE0 do not omit this end-effect and the motion by the restraint. This concludes that the modeling of ITCODE0 elements for purpose of this type of lifetime prediction needs to be revised.

7.3 Hang-off angle assumption

The idea of using an element far down pipe from the BS was that the part should not influence the BS or be influenced by it. A way of saying that it is free from influence is verifying that it has no curvature. However, if the tension is too weak, it will be motions there. It was found that the water was too shallow to impede the changes in curvature. This seen for the curvature envelope in figure 7.2.

Moment and curvature in the elastic range are related linearly $M = EI\kappa$. If probing the value at, say, $x = 30[m]$ from figure 7.2 one will get the pipe's bending stiffness in slip (eq. 7.1). It can be seen that the moment contribution from the bending action down pipe is small compared to the support moment of the BS. It is suggested that the curvature on the line segment down pipe does not influence the BS noticeably.

Even tough the element curves, this should not pose a problem for the hang-off angle assumption. From figure 7.3 it can be seen that the pipe is slightly behind the vessel motion. This suggest that the hang-off angle will be underestimated for half of the cycles while overestimated for the other half. Overall the ranges and mean values will be about the same, but it is indeed clear that this should be evaluated further for the use in shallow water riser systems.

$$\frac{M}{\kappa} = \frac{2644}{0.01163} = 227.34kNm \tag{7.1}$$

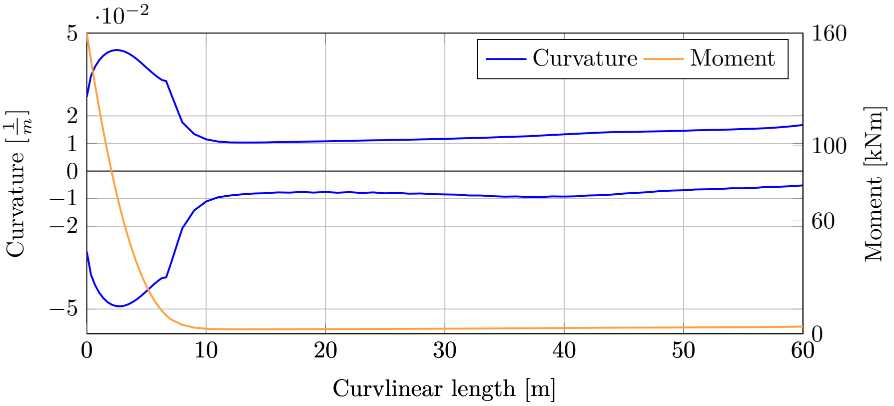

Figure 7.2: Curvature envelope and moment maximum over the first part (LC8)

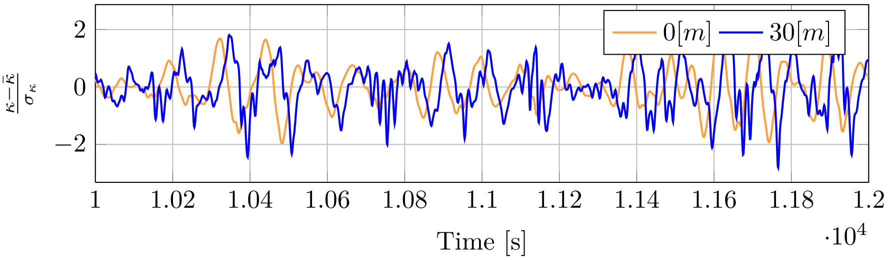

Figure 7.3: Excerpt of the time series of curvature at top and 30 meter down pipe. The values are regularized for comparison by subtracting their mean values and divide on their standard deviation. They show that the curvature of the element down pipe has a slight phase latency.

7.4 Bending stiffener

It was observed, in the global model, that the vertex of the BS should have been around $x \approx 3[m]$. In the local model, it was found closer to the tip. Figure 7.4 demonstrates that a weaker force relocates the vertex further ahead while at the same time shows the tendency to a hinge motion at the tip. Both effects were seen in the BFLEX models.

The dimension of the bending stiffener is exaggerated. It has large support moment of almost $160kNm$ which seems overly excessive for this system. A shorter, but thicker bending stiffener would have given the same curvature with less support moment (Sødahl [1991]). More study in the selection of bending stiffener should clearly have been done. The idea of a fixed length and then solving the contour with static FEM poses the possibility of getting an unnecessary long-stretched bending stiffener. In retrospect it is seen that bending stiffener all the way down to two/three meters could have satisfied the MBR requirement.

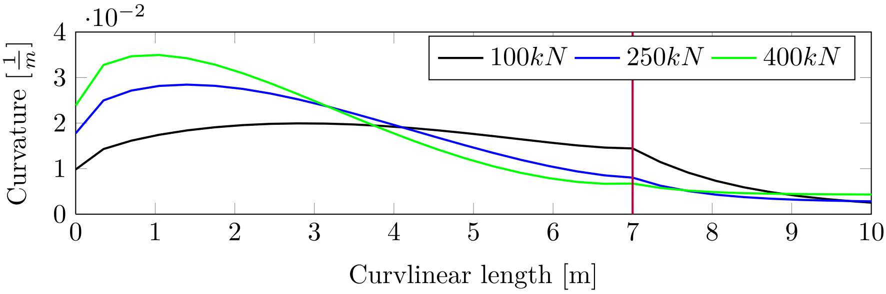

Figure 7.4: Difference in bending stiffener's curvature for different tensions at 8° departure. 2 node elements – static FEM. 250kN is design curve.

7.5 Mesh refinement of M3

- The finer mesh allows to confirm that also the ITCODE0 formulation gives slight damage concentration at the tip.

- It can be readily concluded that the element length does not have a grand impact on the jagged nature of the fatigue distribution for this case.

- The ITCODE0 element defines the helices of the tendons through the 16 integration points around the cross-section, and the numerical integration for every tendon is considered for every point. It is suggested that the response can be smoothed with an increase of integration points around the cross-section.

- The computational time for the case with 200 element over 10 meters is nearly the same as the computational time for M2 which has 30 meters with detailed cross-section. The M3 with 400 elements is the double of this time, without any increase in accuracy.

8 | Conclusions of the study

M1 predicts the lowest lifetime disregarding the hotspot in M3 and the plasticity peak in M2. M1 is much simpler to model and much faster to solve, tough it is more conservative because of the more intense load condition.

M2 and M3 have similar damage aside from their peak fatigues. The BS was found to be too stiff, so large curvature variation is found here. M2 demonstrated this with large damage at the BS-tip. M3 takes account for longitudinal movement of the tendons. It lets the curvature response at the BS-tip be spread further back on the tendons, as such it does not have the high peak fatigue in one or two elements at the BS-tip as the M2 has.

M2 demonstrates a fairly smooth damage distribution over the length of the BS. M3's shear interaction model is inherently more jagged than the moment formulation. M3 had no significant improvement when doubling the number of elements.

M3 has a big damage on the tendons in the area where the bending stiffener starts to curve. It was seen that the elements curve by the wall restraint which is the underlying cause for fatigue response here. This effect was found when modeling the pipe in the same nodal system as the guidetube and BS, and also when the pipe was modeled in a separate nodal system. It is clear that the ITCODE0 element for this type of fatigue calculations needs to be revised and documented further.

Shallow water riser systems have a lot of nonlinear dynamics and effects that are not seen in the deeper water systems. The tension is lower and the relative motion is larger. There was a lot of motion in the hanging section where a reference element was used to calculate the hang-off angle. The consequence is a periodically overestimation and underestimation of the hang-off angle, tough this may not lead to big deviations for the Rainflow counting, which is based on ranges and mean values. However the lack of sufficient tension may cause the riser to get a significant drift already at $x = 30[m]$ if runs were conducted with current. This would compromise the approach. Moreover it was seen that the blocking of the scatter diagram after the responses given in the vessel's RAO was not sufficient. Dynamic trials for wave periods and the riser's hang-off angle should have been conducted instead.

The motivation for using a hang-off angle model instead of a stub model is that it gives a more realistic representation and a less conservative solution.

M3, which uses the ITCODE0 element is interesting. The jagged damage distribution, the high solution time and the hotspot damage found in the root are all arguments that weigh against a recommendation for this element type to be used in commercial projects, in any case the ITCODE0 element should be examined further.

It is important to bring attention to the fact that earlier comparative studies have shown a good correlation between the ITCODE31 element and empirical fatigue tests (ref. section 4.5.2). The predicted life of M2 is almost 51% higher to that of the stub model, disregarding the BS-tip. M2, which used the ITCODE31 elements, is the most promising model for further assessment of fatigue with the hang-off angle and BS-model approach.

9 Recommendation for further work

It is not seldom one will have to repeat certain stages of an analysis one or several times. The accuracy of the angle models depends first and foremost on the accuracy of motion of the model. The BS is too stiff, and simple static FEM with a tension and offset did not serve this project well. In addition the scatter digram was not well blocked. It should be verified that the representative wave inside each block really *is* representative, as commented in the Discussion. It can be questioned if using T_p is the best approach when using the RAO as basis for blocking. The doubt could be omitted entirely by running a dynamic analysis, where the actual response of the system is verified.

To *improve* the current study the author recommends:

- A literature study on BS design, and a redesign of the BS.
- Dynamic trials of harmonic motions to study hang-off angle response should serve as basis for the blocking of the scatter diagram.

A dynamic analysis is suggested to be conducted with the hang-off angle as the governing parameter for blocking. For high hang-off angle response vertical blocking should be performed. To further strengthen this process, a *fictive* fatigue test that uses a harmonic wave given by the representative wave inside each block is thought to help confirm or dismiss the blocking in an early stage. This is more tedious than the path taken in this project, but should improve the blocking. This could prove to save time in comparison of having to redo the irregular runs and cycle-counting because the blocking needed to be adjusted, especially for larger projects which comprise several headings and offsets.

Even tough this study captures the most of fundamental concepts, there is an extensive range of operational conditions which are not accounted for. To *extend* this type of fatigue assessment, the author recommends:

- Add wave spreading and current.
- Assess the different wave headings according to DNV-OS-C102.
- Assess the effect of vessel mean offset on fatigue
- Define the vessel with a well-documented RAO.
- Define the turret and the riser's local position on the vessel.
- Assess the effect of using different BS material, both linear and nonlinear.

appendix A

M3X – ITCODE0 with independent nodal system

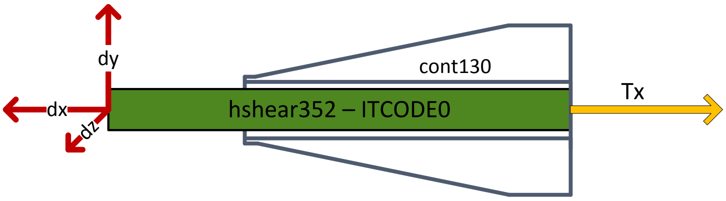

Figure 1: The M3X model in BFLEX. The bending stiffener and pipe are modeled in two independent nodal systems with the same physical coordinates. Displacement is applied instead of forces for numerical stability.

This model was inconclusive, but it is attached as an appendix for reference and further work.

It is thought that the high fatigue response in M3 is from the fact that the bending stiffener and the pipe are modeled in the same nodal system. Here the displacement of the nodes will be dominated by the bending action from the BS elements. To further assess this effect, it was decided to see what happened if the pipe and the BS were modeled in their own nodal systems with contact conditions between them instead. It is then expected that instead of this hotspot damage an equivalent damage would be spread over a larger area avoiding the spike and getting a better result.

Using contact elements in this way is inherently more unstable numerically than using none. Three solutions were possible.

- Model the guidetube in the independent nodal system and use double contact conditions.
- Model the guidetube in the primary nodal system and use constraints in the splice between the guidetube and BS.
- Let the termination of the BS have constant thickness the last 0.5 meters achieving the same bending stiffness as if the guidetube was there.

The last option was chosen. *Cont130* was used as contact element. Additionally no longitudinal nor lateral frictional forces were assumed. This is far from true, as even audible dissipation of energy is heard in physical testing. However, the contact element is not yet suited for this kind of modeling and the author was advised to disregard the feature (Sævik).

The hardness of the contact element was established by demanding a penetration of $0.1[mm]$. The maximum curvature before the tip was found to be $\kappa = 0.04[\frac{1}{m}] \rightarrow \rho = 25000[mm]$ with a corresponding tension of $107kN$

$$q = \frac{T}{\rho}\left[\frac{N}{mm}\right]$$

$$k = \frac{q}{0.1}\left[\frac{N}{mm^2}\right]$$

$$k = \frac{107 \cdot 10}{25} = 42.8\left[\frac{N}{mm^2}\right]$$

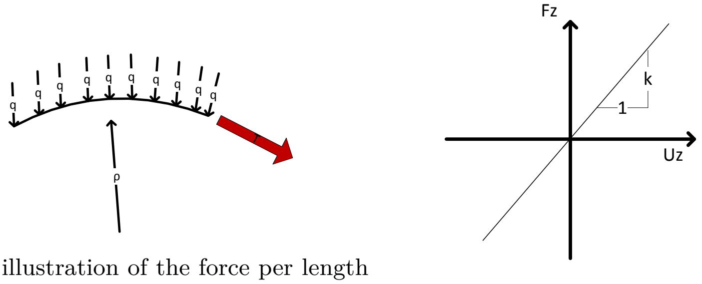

(a) The illustration of the force per length unit – q.

(b) Illustration of the linear hycurve

Figure 2: Illustration of the hardness component of the contact element

It proved difficult to obtain numerical stability for force control in M3X with the same load history as M3. A second attempt, illustrated in figure 1 was tried with the use of prescribed translations dx,dy and dz which are known for M3 on the tip of the ITCODE0 part. The BS was set on fixed support at the root, while the pipe was restrained in the y-direction and given the tension in the opposite direction. Neither this attempt converged.

appendix B

Specific program methodology

The following flowcharts demonstrate the main programs used in this study. Reading and exporting the binary time series data were done using an internal KOGT program. Visual basic scripts were designed by the author to bridge between reading the selected data and preparing them for MarinTek's Rainflow algorithm and re-import these ranges and write out individual BFLEX cases.

It was decided to use separate case files for all the ranges. 38 runs were created. (40 minus 2 zero bins). These were solved simultaneously on eight cores using bat scripts. The post-process however is a single file with all the runs in order where writing is done between the *raf* files. As such this had to be done on a single core. This was however a faster process. The input to LIFETIME contains the actual cycles each run is set to have. It calculates the damage in the same post-result database and accumulates the damage in a separate column as it goes along the list, hence the 38th run has the accumulated damage. Lifetime creates a text-file (*.lof*) which contains the numerical calculations of the damage in every integration point for both layers.

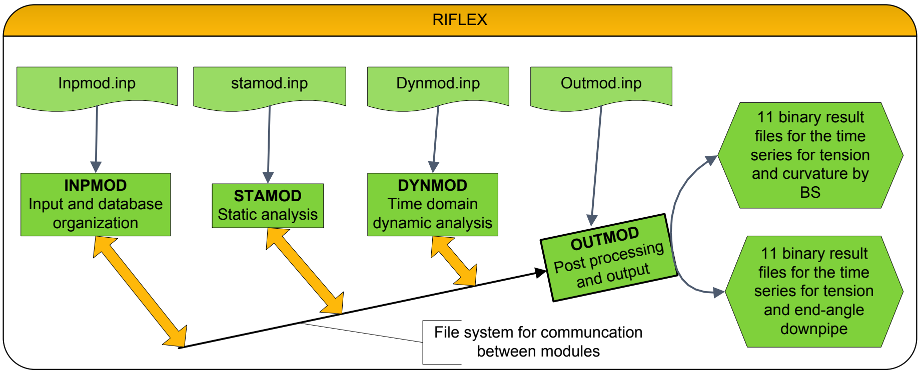

Figure 3: The program outline of RIFLEX

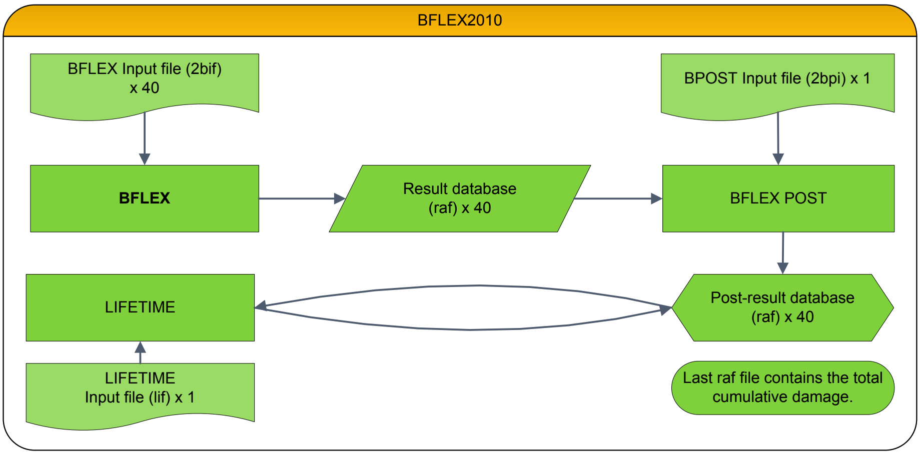

Figure 4: The program outline of BFLEX and BPOST

appendix C

The following is an example of the setup of the Newmark integration.

- β & γ – Weight parameters in the Newmark iteration
- h – The step length, can be constant or variable. Is often dubbed ΔT in FEM.
- r – displacement in t
- $\dot{r}$ – velocity in t
- $\ddot{r}$ – acceleration in t
- M – Mass matrix
- C – The stiffness matrix
- B – The damping matrix

$$\dot{r}_{k+1} = \dot{r}_k + (1-\gamma)h\ddot{r}_k + \gamma h\ddot{r}_{k+1} \tag{1}$$

$$r_{k+1} = r_k + h\dot{r}_k(\frac{1}{2} - \beta)h^2\ddot{r}_k + \beta h^2\ddot{r}_{k+1} \tag{2}$$

By expressing the acceleration and velocity for t_{k+1} with two new displacement vectors a_k and b_k we get:

$$\ddot{r}_{k+1} = \frac{1}{\beta h^2} r_{k+1} - a_k \tag{3}$$

$$\dot{r}_{k+1} = \frac{\gamma}{\beta h^2} r_{k+1} - b_k \tag{4}$$

$$a_k = \frac{1}{\beta h^2} r_k + \frac{1}{\beta h} \dot{r}_k + (\frac{1}{2\beta} - 1)\ddot{r}_k \tag{5}$$

$$b_k = \frac{\gamma}{\beta h^2} r_k + (\frac{\gamma}{\beta} - 1)\dot{r}_k + (\frac{\gamma}{2\beta} - 1)\ddot{r}_k \tag{6}$$

The equation of motion in t_{k+1}:

$$M\ddot{r}_{k+1} + B\dot{r}_{k+1} + Cr_{k+1} = Q_{k+1} \tag{7}$$

Introducing $\hat{C}$ and $\hat{Q}_{k+1}$ as:

$$\hat{C} = C + \frac{\gamma}{\beta h} B + \frac{1}{\beta h^2} M \tag{8}$$

$$\hat{Q}_{k+1} = Q_{k+1} + Bb_k + Ma_k \tag{9}$$

The equilibrium equation can be written as:

$$\hat{C} r_{k+1} = \hat{Q}_{k+1} \tag{10}$$

The acceleration and velocity are promptly found by back-substitution to equations 3 and 4. By this it is seen that $\hat{C}$ is constant for a given step-length.

appendix D

The Rainflow bins for the stub-cases

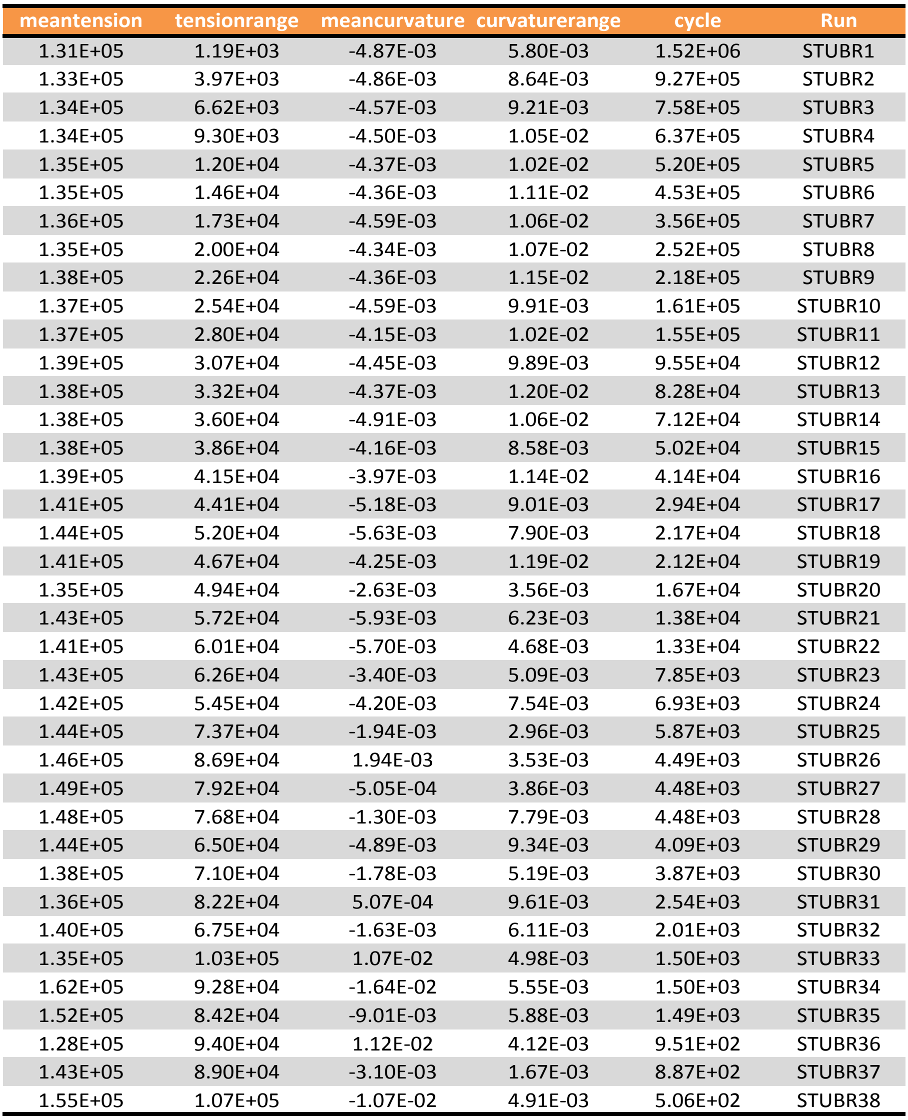

meantension	tensionrange	meancurvature	curvaturerange	cycle	Run
1.31E+05	1.19E+03	-4.87E-03	5.80E-03	1.52E+06	STUBR1
1.33E+05	3.97E+03	-4.86E-03	8.64E-03	9.27E+05	STUBR2
1.34E+05	6.62E+03	-4.57E-03	9.21E-03	7.58E+05	STUBR3
1.34E+05	9.30E+03	-4.50E-03	1.05E-02	6.37E+05	STUBR4
1.35E+05	1.20E+04	-4.37E-03	1.02E-02	5.20E+05	STUBR5
1.35E+05	1.46E+04	-4.36E-03	1.11E-02	4.53E+05	STUBR6
1.36E+05	1.73E+04	-4.59E-03	1.06E-02	3.56E+05	STUBR7
1.35E+05	2.00E+04	-4.34E-03	1.07E-02	2.52E+05	STUBR8
1.38E+05	2.26E+04	-4.36E-03	1.15E-02	2.18E+05	STUBR9
1.37E+05	2.54E+04	-4.59E-03	9.91E-03	1.61E+05	STUBR10
1.37E+05	2.80E+04	-4.15E-03	1.02E-02	1.55E+05	STUBR11
1.39E+05	3.07E+04	-4.45E-03	9.89E-03	9.55E+04	STUBR12
1.38E+05	3.32E+04	-4.37E-03	1.20E-02	8.28E+04	STUBR13
1.38E+05	3.60E+04	-4.91E-03	1.06E-02	7.12E+04	STUBR14
1.38E+05	3.86E+04	-4.16E-03	8.58E-03	5.02E+04	STUBR15
1.39E+05	4.15E+04	-3.97E-03	1.14E-02	4.14E+04	STUBR16
1.41E+05	4.41E+04	-5.18E-03	9.01E-03	2.94E+04	STUBR17
1.44E+05	5.20E+04	-5.63E-03	7.90E-03	2.17E+04	STUBR18
1.41E+05	4.67E+04	-4.25E-03	1.19E-02	2.12E+04	STUBR19
1.35E+05	4.94E+04	-2.63E-03	3.56E-03	1.67E+04	STUBR20
1.43E+05	5.72E+04	-5.93E-03	6.23E-03	1.38E+04	STUBR21
1.41E+05	6.01E+04	-5.70E-03	4.68E-03	1.33E+04	STUBR22
1.43E+05	6.26E+04	-3.40E-03	5.09E-03	7.85E+03	STUBR23
1.42E+05	5.45E+04	-4.20E-03	7.54E-03	6.93E+03	STUBR24
1.44E+05	7.37E+04	-1.94E-03	2.96E-03	5.87E+03	STUBR25
1.46E+05	8.69E+04	1.94E-03	3.53E-03	4.49E+03	STUBR26
1.49E+05	7.92E+04	-5.05E-04	3.86E-03	4.48E+03	STUBR27
1.48E+05	7.68E+04	-1.30E-03	7.79E-03	4.48E+03	STUBR28
1.44E+05	6.50E+04	-4.89E-03	9.34E-03	4.09E+03	STUBR29
1.38E+05	7.10E+04	-1.78E-03	5.19E-03	3.87E+03	STUBR30
1.36E+05	8.22E+04	5.07E-04	9.61E-03	2.54E+03	STUBR31
1.40E+05	6.75E+04	-1.63E-03	6.11E-03	2.01E+03	STUBR32
1.35E+05	1.03E+05	1.07E-02	4.98E-03	1.50E+03	STUBR33
1.62E+05	9.28E+04	-1.64E-02	5.55E-03	1.50E+03	STUBR34
1.52E+05	8.42E+04	-9.01E-03	5.88E-03	1.49E+03	STUBR35
1.28E+05	9.40E+04	1.12E-02	4.12E-03	9.51E+02	STUBR36
1.43E+05	8.90E+04	-3.10E-03	1.67E-03	8.87E+02	STUBR37
1.55E+05	1.07E+05	-1.07E-02	4.91E-03	5.06E+02	STUBR38

The Rainflow bins for the angle-cases.

meantension	tensionrange	anglerange	meanangle	cycle	Run
9.03E+04	8.77E+03	2.12E-01	2.04E-01	9.66E+05	R1
9.07E+04	7.49E+03	2.42E+00	-2.68E-02	4.80E+05	R2
9.11E+04	7.60E+03	3.38E+00	-2.26E-03	4.70E+05	R3
9.06E+04	7.56E+03	4.33E+00	-1.76E-02	4.55E+05	R4
9.07E+04	7.64E+03	5.33E+00	-5.40E-02	3.85E+05	R5
9.05E+04	6.81E+03	1.49E+00	-4.61E-02	3.75E+05	R6
9.09E+04	7.83E+03	6.28E+00	2.01E-02	3.26E+05	R7
9.08E+04	8.48E+03	7.26E+00	-8.70E-03	2.53E+05	R8
9.09E+04	8.26E+03	8.25E+00	4.54E-02	1.91E+05	R9
9.19E+04	8.24E+03	9.19E+00	8.17E-02	1.77E+05	R10
9.18E+04	8.26E+03	1.02E+01	8.34E-02	1.38E+05	R11
9.14E+04	9.36E+03	1.11E+01	8.30E-02	1.14E+05	R12
9.15E+04	1.06E+04	1.21E+01	1.76E-01	8.81E+04	R13
9.17E+04	1.08E+04	1.31E+01	1.56E-01	7.08E+04	R14
8.95E+04	9.61E+03	1.40E+01	1.87E-01	5.86E+04	R15
9.17E+04	9.12E+03	1.50E+01	2.33E-01	5.80E+04	R16
9.14E+04	9.94E+03	1.59E+01	3.02E-01	3.29E+04	R17
9.05E+04	1.03E+04	1.69E+01	2.61E-01	3.23E+04	R18
9.06E+04	8.49E+03	1.79E+01	2.58E-01	2.78E+04	R19
9.17E+04	1.08E+04	1.88E+01	1.57E-01	2.35E+04	R20
9.36E+04	1.08E+04	1.98E+01	-7.93E-02	1.50E+04	R21
9.23E+04	7.36E+03	2.18E+01	2.28E-01	1.41E+04	R22
9.06E+04	9.06E+03	2.07E+01	5.63E-03	1.26E+04	R23
9.02E+04	1.35E+04	2.28E+01	8.54E-02	1.14E+04	R24
8.93E+04	8.47E+03	2.37E+01	1.00E-01	9.35E+03	R25
8.93E+04	8.55E+03	2.46E+01	2.74E-01	7.59E+03	R26
8.78E+04	7.31E+03	2.57E+01	4.53E-01	7.52E+03	R27
9.02E+04	9.67E+03	2.66E+01	3.95E-01	7.27E+03	R28
8.66E+04	1.18E+04	2.77E+01	5.98E-01	5.81E+03	R29
8.98E+04	9.22E+03	2.85E+01	9.06E-01	4.36E+03	R30
8.77E+04	1.01E+04	2.97E+01	7.69E-01	2.72E+03	R31
8.56E+04	1.22E+04	3.17E+01	1.51E+00	2.54E+03	R32
8.19E+04	1.17E+04	3.07E+01	1.08E+00	1.77E+03	R33
9.16E+04	7.60E+03	3.34E+01	1.25E+00	1.33E+03	R34
9.90E+04	2.91E+04	3.56E+01	-4.10E-02	7.59E+02	R35
9.98E+04	3.21E+04	3.62E+01	3.52E-01	5.06E+02	R36
1.02E+05	3.48E+04	3.45E+01	1.10E+00	4.45E+02	R37
9.74E+04	3.17E+04	3.88E+01	2.80E-01	3.81E+02	R38

The translations at pipe-top for 3MX

mm	601			701			801			901			1001		
Cases	dx	dy	dz	dx	dy	dz	dx	dy	dz	dx	dy	dz	dx	dy	dz
3XR1	5.855	68.13	0.711	-185	1659	3.492	4.802	130.3	-0.08	-122	-1333	-4.18	5.857	67.9	0.676
3XR2	6.087	1.304	0.699	-185	1653	3.67	5.755	62.94	-0.22	-148	-1459	-4.46	6.088	1.083	0.707
3XR3	5.961	-33.9	0.627	-169	1583	3.662	6.005	28.08	-0.25	-150	-1469	-4.44	5.961	-34.1	0.634
3XR4	6.057	-4.9	0.862	-209	1751	3.977	5.795	56.14	-0.28	-171	-1558	-4.72	6.057	-5.14	0.908
3XR5	5.83	-45.7	-0.74	-42.4	834.1	2.377	5.948	30.37	0.59	-42	-824	-2.69	5.828	-45.9	-0.75
3XR6	5.975	-17.8	-0.48	-56.4	943	2.736	5.75	55.51	0.514	-49.7	-886	-2.86	5.974	-18.1	-0.5
3XR7	5.884	-45.9	-1.31	-3.41	373.2	0.654	5.814	56.34	1.178	-2.6	-353	-0.78	5.883	-46	-1.33
3XR8	5.876	-44.8	-1.35	-5.85	417.3	0.87	5.804	55.78	1.22	-4.85	-396	-1	5.875	-44.9	-1.37
3XR9	5.937	-26.2	-0.79	-39.5	807.5	2.339	5.781	51.98	0.74	-34.6	-757	-2.54	5.936	-26.4	-0.81
3XR10	5.92	-33.5	-1.25	-15.1	554.3	1.49	5.751	58.36	1.165	-12.4	-512	-1.6	5.919	-33.7	-1.27
3XR11	5.959	-23.9	-1.07	-23	646.6	1.855	5.697	62.44	1.07	-18.6	-592	-1.92	5.958	-24.1	-1.09
3XR12	5.689	75.23	0.682	-160	1528	4.175	4.486	139.5	-0.04	-113	-1287	-3.87	5.693	74.9	0.663
3XR13	5.925	-33.4	-1.32	-12.1	513.4	1.311	5.727	61.5	1.232	-9.41	-470	-1.41	5.924	-33.5	-1.34
3XR14	5.982	-16.7	-0.99	-27.4	693.3	2.013	5.639	67.45	1.028	-21.4	-624	-2.06	5.981	-16.9	-1.01
3XR15	5.871	-43.4	-1.37	-8.4	459	1.072	5.798	54.69	1.235	-7.16	-435	-1.21	5.87	-43.5	-1.39
3XR16	6.053	-9.5	0.066	5.336	106.2	-0.24	6.054	8.57	-0.06	5.292	-104	0.239	6.053	-9.53	0.066
3XR17	5.95	-38.8	-0.77	2.405	234.2	0.027	5.955	38.57	0.633	2.46	-229	-0.16	5.95	-38.9	-0.78
3XR18	5.867	-48.7	-1.27	-1.16	326.5	0.439	5.847	52.67	1.103	-0.77	-314	-0.59	5.867	-48.8	-1.28
3XR19	5.873	-49.7	-1.1	0.908	276.9	0.202	5.916	44.19	0.905	0.832	-275	-0.39	5.872	-49.7	-1.11
3XR20	5.971	-35.1	-0.46	3.833	183.7	-0.16	6.026	21.31	0.287	3.51	-193	-0.03	5.971	-35.2	-0.47
3XR21	6.054	-5.81	0.049	5.753	70.88	-0.15	6.056	1.722	-0.03	5.663	-72.9	0.166	6.054	-5.83	0.049
3XR22	5.962	-18.6	-0.85	-35.8	773.4	2.289	5.684	61.43	0.855	-29.9	-712	-2.39	5.961	-18.8	-0.88
3XR23	5.853	-38	-0.66	-47.1	870.9	2.56	5.875	37.26	0.562	-45.2	-848	-2.82	5.852	-38.2	-0.68
3XR24	6.028	-20.1	-0.12	4.733	142.3	-0.24	6.042	13.91	0.044	4.616	-145	0.16	6.028	-20.1	-0.12
3XR25	6.054	-2.79	0.006	5.979	39.74	-0.07	6.054	-2.58	0.005	5.892	-43.9	0.078	6.054	-2.81	0.006
3XR26	5.96	-19.3	-0.94	-31.3	731.8	2.148	5.672	62.84	0.948	-25.5	-667	-2.25	5.959	-19.5	-0.97
3XR27	6.043	11.43	-0.02	6.072	17.68	-0.03	6.043	11.43	-0.02	6.01	5.388	-0.01	6.043	11.43	-0.02
3XR28	5.994	-1.13	-0.02	-89.2	1161	3.322	5.605	67.74	0.251	-74.9	-1063	-3.41	5.994	-1.37	-0.05
3XR29	5.899	-29.4	-0.47	-60.5	973.7	2.77	5.828	43.28	0.419	-54.8	-922	-3.13	5.898	-29.6	-0.49
3XR30	5.908	43.6	0.258	-111	1286	3.632	5	111.1	0.201	-80.9	-1101	-3.51	5.909	43.32	0.226
3XR31	5.913	-29.8	-1.21	-18.5	594.8	1.695	5.706	59.88	1.15	-15.1	-548	-1.79	5.912	-30	-1.22
3XR32	5.898	-28.1	-0.37	-65.5	1007	2.979	5.815	43.64	0.385	-60.7	-966	-3.18	5.897	-28.3	-0.38
3XR33	5.961	-12.7	-0.24	-73.6	1061	3.123	5.693	58.11	0.363	-64.1	-990	-3.24	5.96	-12.9	-0.26
3XR34	5.976	2.784	-0.11	-82	1114	3.328	5.521	72.97	0.342	-67.8	-1015	-3.33	5.976	2.533	-0.13
3XR35	5.938	31.45	0.336	-117	1316	3.765	5.174	98.8	0.104	-89.3	-1150	-3.72	5.939	31.18	0.301
3XR36	5.962	15.96	0.105	-99.1	1217	3.527	5.359	84.93	0.221	-77.3	-1075	-3.61	5.962	15.72	0.076
3XR37	5.423	94.38	0.611	-146	1459	4.123	3.914	161.2	0.112	-91.2	-1158	-3.88	5.427	94.09	0.593
3XR38	5.761	55.6	0.468	-128	1366	4.116	4.672	124.1	0.153	-88.8	-1141	-3.92	5.763	55.35	0.475

References

ASTM International. E1049-85 - standard practices for cycle counting in fatigue analysis. 1985. Reapproved 2005. 45

J.L. Robert J. Bahuaud C. Amzallag, J.P. Gerey. Standardization of the rainflow counting method for fatigue analysis. 1993. 45, 46

Tim Crome. Smoothbore flexible riser for gas export (statoil operated Åsgard field). *Offshore Technology Conference*, April 2007. 5

DNV. Dnv-os-c102. October 2011. Structural Design of Offshore Ships. 53, 57

Gassco. http://www.gassco.no/wps/wcm/connect/gassco-en/gassco/home/var-virksomhet/ror-og-plattformer/langeled. 4

ISO. *ISO13628-11:2007 Flexible pipe systems for subsea and marine applications*. ISO, 2007. xiii, 7, 8, 17

Ragnar Sigbjornsson Ivar Langen. *Dynamic Response of Marine Structures*. Institutt for Marin Teknikk, 2010. 38

MCS Kenny. State of the art report on flexible pipe integrity and guidance note on monitoring methods and integrity assurance for unbonded flexible pipes. Technical Report OP010, 2010. 15

Rolf Hugo Kirkvik. Flexible pipe on-seabed stability, upheaval buckling and hub protection methods. 2013. 32

Offshore.no. News article: http://www.offshore.no/sak/35892_skrugardkonsept_tar_form. 15

Andrew C Palmer. *Subsea Pipeline Engineering, 2nd Edition*, page 173. Pennwell, Kidlington, Oxford, 2008. 5

Prof. Svein Sævik. Personal communication. 17, 43, 47, 57, II

Prof. Svein Sævik. *BFLEX 2010 theory manual 3.19v1*. MarinTek, March 2000. xiv, 41

Prof. Svein Sævik. Lecure notes in offshore pipeline technology. for support of the course Pipeline Technology given at the Institute of Marine Technology, September 2012a. xiv, 24, 25, 27, 29, 35, 36

Prof. Svein Sævik. *Simla 3.16.0 usermanual*. MarinTek, October 2012b. xiv, 24

Prof. Svein Sævik. *BFLEX 2010 user manual 3.0.7*. MarinTek, February 2013. 17, 41, 74

Nils Sødahl. *Methods for design and analysis of flexible risers*, pages 62–77. Department of Marine Technology, NTNU, June 1991. 93

noteVol. 27, No. 5, pp. 651-662 (2004) publisher=Chinese Institute of Engineers year=2004 Shuenn-Yih Chang, title=Studies of Newmark Method for solving nonlinear systems (I) Basic Analysis. 38

Society for Underwater Technology SUT. The life-cycle of flexible risers and flowlines. March 2012. The conference material was provided as coursework as an introduction to flexibles to the author by KOGT. 19

Technip. Technip's presentation Flexible Pipe at http://www.technip.com/en/our-business/subsea/flexible-pipe. 14

TMB. http://www.timemoneyandblood.com/HTML/normandy/operation-pluto/operation-pluto.html. 14

Trelleborg. News article: http://www.trelleborg.com/en/Media/Products-and-Solutions-News/Archive/Trelleborg-strengthens-position-by-acquiring-established-syntactic-foam-business-in-UK/. 15

Y. Zhang. State of the art analytical tools improve optimization of unbonded flexible pipes for deepwater environments. *Offshore Technology Conference*, 158, 2003. figure 1, page 1. xiii, 6